

Strong-field QED effects on polarization states in dipole and quadrudipole pulsar emissions

Dong-Hoon Kim^{a,b} Chul Min Kim^c Sang Pyo Kim^{d,e}

^aThe Research Institute of Basic Science, Seoul National University, Seoul 08826, Republic of Korea

^bDepartment of Physics and Astronomy, Seoul National University, Seoul 08826, Republic of Korea

^cAdvanced Photonics Research Institute, Gwangju Institute of Science and Technology, Gwangju 61005, Republic of Korea

^dDepartment of Physics, Kunsan National University, Gunsan 54150, Republic of Korea

^eAsia Pacific Center for Theoretical Physics, Pohang 37673, Republic of Korea

E-mail: ki13130@gmail.com, chulmin@gist.ac.kr, sangkim@kunsan.ac.kr

Abstract. Highly magnetized neutron stars have quantum refraction effects on pulsar emission due to the non-linearity of the quantum electrodynamics (QED) action. In this paper, we investigate the evolution of the polarization states of pulsar emission under the quantum refraction effects, combined with the dependence on the emission frequency; we solve a system of evolution equations of the Stokes vector, where the birefringent vector, in which such effects are encoded, acts on the Stokes vector. At a fixed frequency of emission, depending on the magnitude of the birefringent vector, dominated mostly by the magnetic field strength, the evolution of the Stokes vector largely exhibits three different patterns: (i) monotonic, or (ii) half-oscillatory, or (iii) highly oscillatory behaviors. These features are understood and confirmed by means of approximate analytical solutions to the evolution equations.

Keywords: pulsars, magnetic fields, photon emission, photon polarization, nonlinear electrodynamics, nonlinear vacuum, vacuum birefringence, quantum refraction, polarization evolution

ArXiv ePrint: [2406.05752](https://arxiv.org/abs/2406.05752)

Contents

1	Introduction	1
2	Evolution of polarization states in strong magnetic field – dipole pulsars	3
2.1	Evolution equations of Stokes vector	3
2.2	Solving the evolution equations	7
2.2.1	Examples	8
2.2.2	Approximate analytical solutions	9
3	Evolution of polarization states in strong magnetic field – quadrupole pulsars	14
3.1	Modified magnetic field geometry and evolution equations of Stokes vector	14
3.2	Solving the evolution equations	18
3.2.1	Examples	18
4	Conclusions and discussion	19
A	The classical Stokes vector	23
B	Approximate analytical solutions to evolution equations	25

1 Introduction

Strong fields may open a window for testing fundamental physics. Even before quantum electrodynamics (QED) was fully developed and precisely tested in the weak field regime, Heisenberg and Euler showed that a strong electromagnetic field can polarize the Dirac vacuum [1]. Schwinger introduced the proper-time integral method to obtain the one-loop effective QED action of the vacuum under a uniform electromagnetic field [2]. The so-called Heisenberg-Euler-Schwinger (HES) action provides an effective theory of electrodynamics in strong fields, in which the linear Maxwell vacuum is turned into a dielectric medium with electric, magnetic, and magneto-electric responses. Consequently, a photon propagating in a region of strong electromagnetic fields can experience vacuum birefringence, i.e., a quantum refraction effect [3]. Furthermore, when the electric field is sufficiently strong to be comparable to the critical electric field strength ($E_c = m_e^2 c^3 / (e\hbar) = 1.3 \times 10^{18}$ V/m), electron-positron pairs can be created spontaneously out of the vacuum, which is called Sauter-Schwinger pair production [4–6]. Observing these effects will validate the quantum vacuum model in the strong-field regime; however, vacuum birefringence is practically far more likely to be implemented or observed than Sauter-Schwinger pair production.

Although the relevant field strength is too high to attain by terrestrial means, an experiment and several proposals for testing strong-field QED have been reported. In the PVLAS (Polarizzazione del Vuoto con Laser, i.e., polarization of vacuum with laser) project, permanent, superconducting magnets have been used with laser as a probe, and a limit on vacuum birefringence has been reported for a field strength of 2.5 T [7]. Recently, several proposals have appeared, in which ultra-intense laser fields are used with x-rays as a probe

[8–10]; the current ultra-intense laser can provide a magnetic field strength of 10^6 T [5]. Although the fields from such lasers are still weaker than the critical magnetic field strength, $B_c = m_e^2 c^3 / e \hbar = 4.4 \times 10^{13}$ G by three orders, these proposals are promising for the observation of vacuum birefringence in the relatively weak-field regime. Thus, they are seriously considered to be conducted at upcoming ultra-intense laser facilities [11].

However, the observation of vacuum birefringence in the strong-field regime requires a field strength comparable to the critical value. It has been predicted that such extreme fields are available from astrophysical compact objects. For instance, highly magnetized neutron stars have magnetospheres whose field strength approaches up to 10^{11} T (about 50 times as high as the critical field strength) [3, 12]. In this regard, several space telescope missions are being conducted or proposed to observe the X-rays from neutron stars for vacuum birefringence: the Imaging X-ray Polarimetry Explorer [13], the enhanced X-ray Timing and Polarimetry (eXTP) [14] and the Compton Telescope project [15]. The X-rays from a neutron star contain information about vacuum birefringence in its magnetosphere, and the birefringence effect accumulates over the magnetospheric size. Such accumulation is a great advantage compared to terrestrial laser experiments, not to mention the available field strength. This way, astrophysical compact objects can be used as a laboratory to test fundamental physics in the strong-field regime [3, 16].

The HES action is well approximated by the post-Maxwellian action, even up to the strength one order lower than the critical magnetic field B_c , which keeps up to the quadratic terms of the Maxwell scalar and pseudo-scalar. Therefore, the post-Maxwellian action exhibits non-linear characteristics of vacuum polarization, such as quantum refraction [17–19]. Previously, we have studied the quantum refraction effects on the propagation of a probe photon in the magnetic dipole field background of a pulsar model [20]. The study is non-trivial in comparison with other similar studies wherein the background magnetic field is assumed to be uniform, in that we have to deal with a dipole magnetic field, the strength and direction of which vary over space. However, recent observations suggest the importance of studies regarding multipolar structures of the magnetic fields in pulsars [21–24].

In this work, we investigate the evolution of the polarization states of pulsar emission under the quantum refraction effects, combined with the dependence on the emission frequency, for dipole and quadrupole (for the first time, to our knowledge) pulsar models. To this end, we employ the evolution equations of the Stokes vector, where such effects are encoded into the birefringent vector that acts on the Stokes vector. The Stokes vector has a crucial advantage over the polarization vector in representing polarization states: it can be directly determined from experimentally measurable quantities and accommodate depolarization effects due to incomplete coherence and random processes during the photon propagation. Solutions of the evolution equations describe how the polarization states change along the photon propagation path from the emission point towards an observer. It turns out that the evolution of the Stokes vector, at a fixed frequency of emission, largely exhibits three different patterns, depending on the magnitudes of the birefringent vector, dominated mostly by the magnetic field strength: (i) fractionally oscillatory - monotonic, or (ii) half-oscillatory, or (iii) highly oscillatory behaviors, which are found by numerical solutions and also confirmed by approximate analytical solutions. These are novel features rarely illuminated in previous studies on the same topic. In addition, it is investigated how the aforementioned features regarding the evolution of the Stokes vector change as we replace a dipole field with a quadrupole field to modify the pulsar magnetic field structure. Throughout our analysis, X-ray emission from pulsars, with frequency $\sim 10^{18}$ Hz, is considered; in this regime, the vacuum contribution

to the birefringence dominates that of the plasma [25, 26]. Also, our analysis is sufficiently rigorous in solving the evolution equations of the Stokes vector, into which we feed precise information of photon propagation under the pulsar rotation effect.

The paper is organized as follows. In section 2.1, we introduce a system of evolution equations of the Stokes vector and apply this formalism to our pulsar emission model for an oblique dipole rotator. In section 2.2, the evolution equations are solved for some known rotation-powered pulsars (RPPs) in three ways: fully numerically, via perturbation analysis, and using an analytical approximation. Also, we discuss the evolution patterns of the Stokes vectors resulting from the solutions. In section 3.1, we consider a magnetic quadrupole model for pulsar emission and look into the evolution equations under this model. In section 3.2, we solve the evolution equations for the same RPPs fully numerically, and compare the results with those for the dipole case in section 2.2. Then finally, we conclude the paper with discussions on other similar studies and future follow-up studies.

2 Evolution of polarization states in strong magnetic field – dipole pulsars

2.1 Evolution equations of Stokes vector

Classically, polarization properties of pulsar emission are described by the Stokes parameters $\{I, Q, U, V\}$, where I is a measure of the total intensity, Q and U jointly describe the linear polarization, and V describes the circular polarization of the curvature emission in pulsars (for more details, see Appendix A). However, in the presence of a strong magnetic field in the background of the emission, the polarization evolves along the photon propagation path from the emission point towards an observer. The evolution of the polarization can be investigated systematically using the formalism initiated by [27–29], and further developed by [25, 30–32], namely, a system of evolution equations of the Stokes vector, described as

$$\frac{d\mathbf{S}}{ds} = k\hat{\Omega} \times \mathbf{S}, \quad (2.1)$$

where $k \equiv \omega/c$ denotes the wave number for the electromagnetic radiation and s is an affine parameter to measure the length of the photon trajectory, and \mathbf{S} is the normalized Stokes vector, defined out of the Stokes parameters as $\mathbf{S} = (S_1, S_2, S_3) \equiv (Q/I, U/I, V/I)$,¹ and $\hat{\Omega}$ is the *dimensionless* birefringent vector, defined as²

$$\hat{\Omega} \equiv \frac{\alpha_e}{30\pi} (B/B_c)^2 \sin^2 \vartheta (\mathcal{E}_I^2 - \mathcal{E}_{II}^2, 2\mathcal{E}_I\mathcal{E}_{II}, 0), \quad (2.2)$$

where α_e denotes the fine-structure constant and $\alpha_e/(30\pi) \approx 7.743 \times 10^{-5}$ and $B_c \approx 4.414 \times 10^{13}$ G is the critical magnetic field, and ϑ denotes the angle between the photon trajectory and the local magnetic field line (see figure 1), i.e.,

$$\vartheta = \cos^{-1}(\hat{\mathbf{n}}_{[0]} \cdot \hat{\mathbf{B}}), \quad (2.3)$$

with $\hat{\mathbf{n}}_{[0]}$ being the classical propagation vector and $\hat{\mathbf{B}} \equiv \mathbf{B}/|\mathbf{B}|$, and

$$\mathcal{E}_i \equiv -\hat{\mathbf{B}} \cdot (\hat{\mathbf{n}}_{[0]} \times \boldsymbol{\varepsilon}_{i[0]}), \quad i = \text{I, II}, \quad (2.4)$$

¹The classical Stokes vector can be expressed via pulse profiles of pulsar curvature emission, as illustrated in Appendix A.

²Note that our $k\hat{\Omega}$ is equivalent to the birefringent vector as defined in the references above.

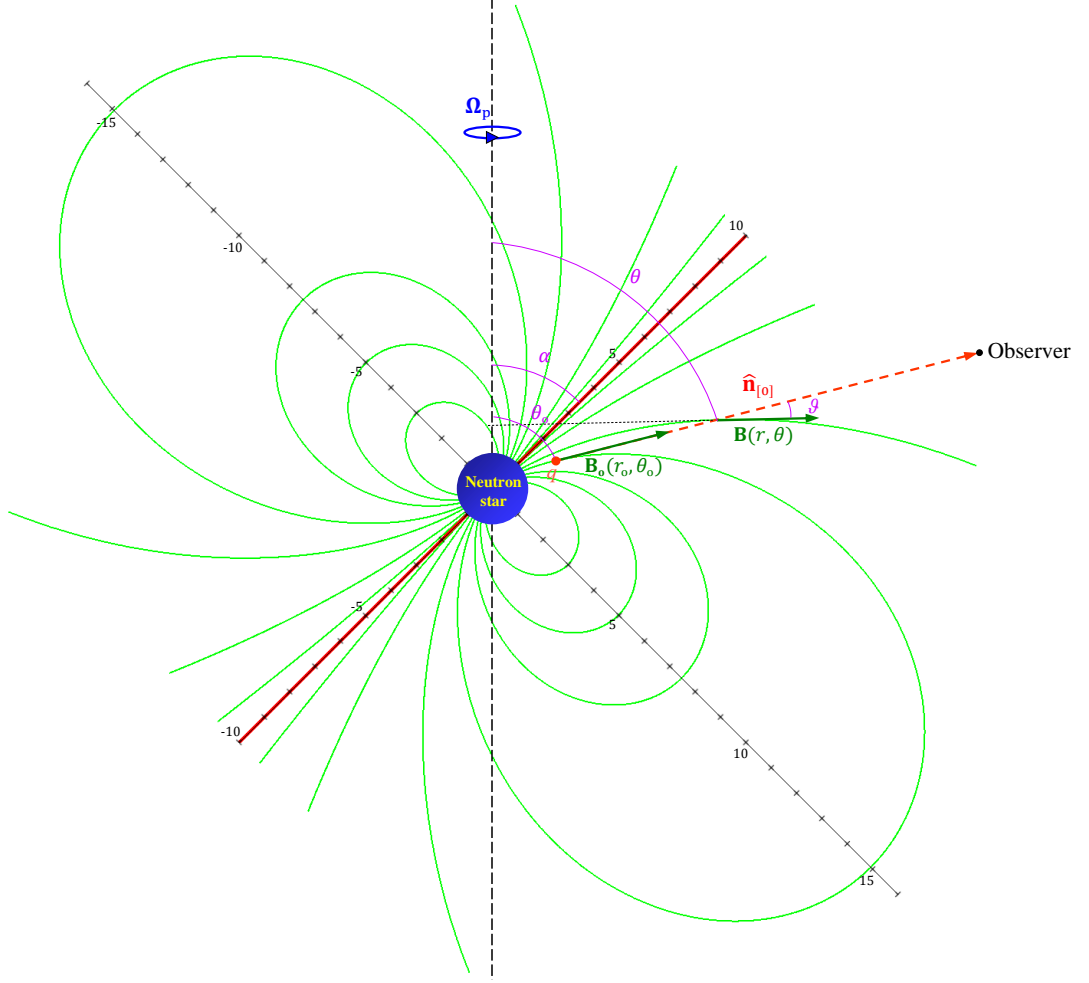


Figure 1: A cross-sectional view of a pulsar magnetosphere with the dipole magnetic field lines (green) around a neutron star. The vertical dashed line (black) and the inclined solid line (red) represent the rotation axis and the magnetic axis, respectively. α between these axes denotes the inclination angle. The scale of the unity in this graph is equivalent to the neutron star radius $\sim 10^6$ cm. The red dashed line represents the trajectory curve of the light ray traced by the propagation vector $\hat{\mathbf{n}}_{[0]}$ as projected onto the xz -plane. (Credit: [33], reproduced with modifications.)

with $\boldsymbol{\varepsilon}_{\text{I}[0]}$ and $\boldsymbol{\varepsilon}_{\text{II}[0]}$ being the two classical mode polarization vectors, orthogonal to each other and to $\hat{\mathbf{n}}_{[0]}$; the specific forms of $\hat{\mathbf{n}}_{[0]}$, $\boldsymbol{\varepsilon}_{\text{I}[0]}$ and $\boldsymbol{\varepsilon}_{\text{II}[0]}$ are later given by eqs. (2.8), (2.12) and (2.13), respectively, for the magnetic field of an oblique dipole rotator as described by eq. (2.5) and figure 1.

In our pulsar emission model, we consider curvature radiation produced along the magnetic field lines of an oblique dipole rotator as illustrated in figure 1:

$$\mathbf{B}(r, \theta, \phi) = \frac{2\mu(\cos \alpha \cos \theta + \sin \alpha \sin \theta \cos \phi)}{r^3} \mathbf{e}_{\hat{r}} + \frac{\mu(\cos \alpha \sin \theta - \sin \alpha \cos \theta \cos \phi)}{r^3} \mathbf{e}_{\hat{\theta}} + \frac{\mu \sin \alpha \sin \phi}{r^3} \mathbf{e}_{\hat{\phi}}, \quad (2.5)$$

where μ is the magnetic dipole moment and α denotes the inclination angle between the rotation axis and the magnetic axis.³ The photon beam from curvature radiation is tangent to the field line at the emission point $(x_o, y_o, z_o) = (r_o \sin \theta_o, 0, r_o \cos \theta_o)$.

However, at the same time, our pulsar magnetosphere rotates, and therefore the field lines get twisted due to the magneto-centrifugal acceleration on the plasma particles moving along the field lines [34]. Then, taking into consideration this magneto-hydrodynamic (MHD) effect, the direction of the classical photon propagation, which must line up with the particle velocity in order for an observer to receive the radiation, can be described as [35]

$$\hat{\mathbf{n}}_{[0]} = \beta \hat{\mathbf{B}} + \frac{\boldsymbol{\Omega}_p \times \mathbf{r}}{c}, \quad (2.6)$$

where on the right-hand side

$$\beta \equiv \left[1 - \left(\frac{\Omega_p r}{c} \right)^2 \sin^2 \theta \left(1 - \frac{\sin^2 \alpha \sin^2 \phi}{3 \cos^2 \theta' + 1} \right) \right]^{1/2} - \frac{\Omega_p r}{c} \frac{\sin \alpha \sin \theta \sin \phi}{(3 \cos^2 \theta' + 1)^{1/2}}, \quad (2.7)$$

with c being the speed of light and $\cos \theta' \equiv \cos \alpha \cos \theta + \sin \alpha \sin \theta \cos \phi$, and the second term accounts for the centrifugal acceleration, with $\boldsymbol{\Omega}_p \equiv \Omega_p \mathbf{e}_z$ ⁴ and $\Omega_p = 2\pi/P$ being a pulsar rotation (angular) frequency, as given in terms of the rotation period P .

During the rotation the azimuthal phase changes by $\phi \sim \Omega_p t$, while our photon has propagated a distance by $s \sim ct$. In our analysis, the photon propagation is described with the consideration of the MHD effect above, assuming ϕ to be very small; e.g., $\phi \lesssim 10^{-1}$ is considered for a millisecond pulsar with $\Omega_p \sim 10^2$ Hz, during the time of rotation $t \lesssim 10^{-3}$ s, such that $s \lesssim 10^7$ cm, which corresponds to the propagation distance within about 10 times the neutron star radius. For eq. (2.6) we take only the leading order expansions of $\hat{\mathbf{B}}(r_o, \theta_o, \phi)$ and $\beta(r_o, \theta_o, \phi)$ in ϕ from eqs. (2.5) and (2.7), respectively, and can express the classical propagation vector $\hat{\mathbf{n}}_{[0]}$ in Cartesian coordinates as

$$\hat{\mathbf{n}}_{[0]} = \hat{n}_{x[0]} \mathbf{e}_x + \hat{n}_{y[0]} \mathbf{e}_y + \hat{n}_{z[0]} \mathbf{e}_z \quad (2.8)$$

with

$$\hat{n}_{x[0]} \approx \frac{2 \cos(\theta_o - \alpha) \sin \theta_o + \sin(\theta_o - \alpha) \cos \theta_o}{(3 \cos^2(\theta_o - \alpha) + 1)^{1/2}} + \mathcal{O}\left(\phi^2, (\Omega_p r_o/c)^2, \phi(\Omega_p r_o/c)\right), \quad (2.9)$$

$$\hat{n}_{z[0]} \approx \frac{2 \cos(\theta_o - \alpha) \cos \theta_o - \sin(\theta_o - \alpha) \sin \theta_o}{(3 \cos^2(\theta_o - \alpha) + 1)^{1/2}} + \mathcal{O}\left(\phi^2, (\Omega_p r_o/c)^2, \phi(\Omega_p r_o/c)\right), \quad (2.10)$$

and

$$\hat{n}_{y[0]} \approx \frac{\Omega_p}{c} \left[\frac{\sin \alpha s}{(3 \cos^2(\theta_o - \alpha) + 1)^{1/2}} + r_o \sin \theta_o \right] + \mathcal{O}\left(\phi^2, (\Omega_p r_o/c)^2, \phi(\Omega_p r_o/c)\right), \quad (2.11)$$

where we have considered $\Omega_p r_o/c \lesssim \phi$, e.g., for a millisecond pulsar with $\Omega_p \sim 10^2$ Hz and $r_o \sim 10^6$ cm, such that $(\Omega_p r_o/c)^2 \lesssim \phi(\Omega_p r_o/c) \lesssim \phi^2$, all to be ignored in our analysis, and have substituted $\phi = \Omega_p s/c$ in eq. (2.11), the leading order rotational effect to be considered in our analysis.

³Here the symbol α must be distinguished from the fine-structure constant α_e .

⁴Here the symbol $\boldsymbol{\Omega}_p$ must be distinguished from the birefringent vector $\hat{\boldsymbol{\Omega}}$.

The orthogonal pair of classical mode polarization vectors, $\boldsymbol{\varepsilon}_{\text{I}[0]}$ and $\boldsymbol{\varepsilon}_{\text{II}[0]}$, both being also orthogonal to $\hat{\mathbf{n}}_{[0]}$ as given by eq. (2.8) above, are determined as

$$\boldsymbol{\varepsilon}_{\text{I}[0]} = \hat{n}_{z[0]}\mathbf{e}_x + \hat{n}_{y[0]}\mathbf{e}_y - \hat{n}_{x[0]}\mathbf{e}_z, \quad (2.12)$$

$$\boldsymbol{\varepsilon}_{\text{II}[0]} = -(\hat{n}_{x[0]} + \hat{n}_{z[0]})\hat{n}_{y[0]}\mathbf{e}_x + \mathbf{e}_y + (\hat{n}_{x[0]} - \hat{n}_{z[0]})\hat{n}_{y[0]}\mathbf{e}_z, \quad (2.13)$$

such that the three vectors, $\hat{\mathbf{n}}_{[0]}$, $\boldsymbol{\varepsilon}_{\text{I}[0]}$ and $\boldsymbol{\varepsilon}_{\text{II}[0]}$ form an orthonormal basis.⁵ Using these for eq. (2.4), we obtain

$$\begin{aligned} \mathcal{E}_{\text{I}} &= -\hat{\mathbf{B}} \cdot (\hat{\mathbf{n}}_{[0]} \times \boldsymbol{\varepsilon}_{\text{I}[0]}) \\ &\approx \frac{4 \cos(\theta_o - \alpha) \cos(\theta - \alpha) + \sin(\theta_o - \alpha) \sin(\theta - \alpha) + 2 \sin(\theta - \theta_o)}{(3 \cos^2(\theta_o - \alpha) + 1)^{1/2} (3 \cos^2(\theta - \alpha) + 1)^{1/2}} \hat{n}_{y[0]} \\ &\quad - \frac{\Omega_p \sin \alpha s}{c (3 \cos^2(\theta - \alpha) + 1)^{1/2}} + \mathcal{O}\left(\phi^2, (\Omega_p r_o/c)^2, \phi(\Omega_p r_o/c)\right), \end{aligned} \quad (2.14)$$

$$\begin{aligned} \mathcal{E}_{\text{II}} &= -\hat{\mathbf{B}} \cdot (\hat{\mathbf{n}}_{[0]} \times \boldsymbol{\varepsilon}_{\text{II}[0]}) \\ &\approx -\frac{2 \sin(\theta - \theta_o)}{(3 \cos^2(\theta_o - \alpha) + 1)^{1/2} (3 \cos^2(\theta - \alpha) + 1)^{1/2}} \\ &\quad + \mathcal{O}\left(\phi^2, (\Omega_p r_o/c)^2, \phi(\Omega_p r_o/c)\right). \end{aligned} \quad (2.15)$$

By means of eqs. (2.3), (2.5) and (2.8) one can express

$$\begin{aligned} \cos \vartheta &\approx \frac{4 \cos(\theta_o - \alpha) \cos(\theta - \alpha) + \sin(\theta_o - \alpha) \sin(\theta - \alpha)}{(3 \cos^2(\theta_o - \alpha) + 1)^{1/2} (3 \cos^2(\theta - \alpha) + 1)^{1/2}} \\ &\quad + \mathcal{O}\left(\phi^2, (\Omega_p r_o/c)^2, \phi(\Omega_p r_o/c)\right), \end{aligned} \quad (2.16)$$

$$\begin{aligned} \sin \vartheta &\approx \frac{2 \sin(\theta - \theta_o)}{(3 \cos^2(\theta_o - \alpha) + 1)^{1/2} (3 \cos^2(\theta - \alpha) + 1)^{1/2}} \\ &\quad + \mathcal{O}\left(\phi^2, (\Omega_p r_o/c)^2, \phi(\Omega_p r_o/c)\right). \end{aligned} \quad (2.17)$$

Now, using the relations between eqs. (2.14)-(2.17), the birefringent vector can finally be specified from eq. (2.2):

$$\hat{\Omega}_1 \approx -\eta B^2 \sin^4 \vartheta + \mathcal{O}\left(\phi^2, (\Omega_p r_o/c)^2, \phi(\Omega_p r_o/c)\right), \quad (2.18)$$

$$\begin{aligned} \hat{\Omega}_2 &\approx -2\eta B^2 \sin^3 \vartheta \left[(\cos \vartheta + \sin \vartheta) \hat{n}_{y[0]} - \frac{\Omega_p \sin \alpha s}{c (3 \cos^2(\theta - \alpha) + 1)^{1/2}} \right] \\ &\quad + \mathcal{O}\left(\phi^2, (\Omega_p r_o/c)^2, \phi(\Omega_p r_o/c)\right), \end{aligned} \quad (2.19)$$

where $\eta \equiv \alpha_e / (30\pi B_c^2)$ and

$$B = \frac{B_{\text{max}} r_*^3 (3 \cos^2(\theta - \alpha) + 1)^{1/2}}{2(x^2 + z^2)^{3/2}}, \quad (2.20)$$

⁵It can be checked out that $\hat{\mathbf{n}}_{[0]} \cdot \boldsymbol{\varepsilon}_{\text{I}[0]} \approx 0 + \mathcal{O}((\Omega_p r_o/c)^2)$, $\hat{\mathbf{n}}_{[0]} \cdot \boldsymbol{\varepsilon}_{\text{II}[0]} = 0$ and $\boldsymbol{\varepsilon}_{\text{I}[0]} \cdot \boldsymbol{\varepsilon}_{\text{II}[0]} = 0$ while $\hat{\mathbf{n}}_{[0]}^2 \approx 1 + \mathcal{O}((\Omega_p r_o/c)^2)$ and $\boldsymbol{\varepsilon}_{\text{I,II}[0]}^2 \approx 1 + \mathcal{O}((\Omega_p r_o/c)^2)$.

with B_{\max} being the maximum magnetic field intensity at the polar cap⁶ and r_* being the neutron star radius ($\approx 10^6$ cm), and $\hat{n}_{y[0]}$, $\cos \vartheta$ and $\sin \vartheta$ are given by eqs. (2.11), (2.16) and (2.17), respectively.

To facilitate solving the evolution equation (2.1) in the next subsection, we substitute the following identities,

$$\cos(\theta - \alpha) = \frac{\sin \alpha x + \cos \alpha z}{(x^2 + z^2)^{1/2}}, \sin(\theta - \alpha) = \frac{\cos \alpha x - \sin \alpha z}{(x^2 + z^2)^{1/2}}, \sin(\theta - \theta_o) = \frac{\cos \theta_o x - \sin \theta_o z}{(x^2 + z^2)^{1/2}}, \quad (2.21)$$

together with

$$x = \hat{n}_{x[0]}s + r_o \sin \theta_o, \quad z = \hat{n}_{z[0]}s + r_o \cos \theta_o \quad (2.22)$$

into (2.16) and (2.17). Then our solutions for the Stokes vector \mathbf{S} will be parameterized solely by s .

2.2 Solving the evolution equations

From eq. (2.1) we write down a system of first-order ordinary differential equations to solve:

$$\dot{S}_1(s) = k\hat{\Omega}_2(s)S_3(s), \quad (2.23)$$

$$\dot{S}_2(s) = -k\hat{\Omega}_1(s)S_3(s), \quad (2.24)$$

$$\dot{S}_3(s) = k \left[\hat{\Omega}_1(s)S_2(s) - \hat{\Omega}_2(s)S_1(s) \right], \quad (2.25)$$

where an over-dot denotes differentiation with respect to s , and $\hat{\Omega}_1(s)$ and $\hat{\Omega}_2(s)$ are given by (2.18) and (2.19), respectively. By solving these equations numerically, we find out how the photon polarization evolves through the strong magnetic field in the background of our pulsar emission.

However, in case $\left| k\hat{\Omega}_{1,2}(s)s \right|_{\max} \ll 1$, one can obtain a solution to eq. (2.1) via perturbation:

$$\mathbf{S} = \mathbf{S}_{[0]} + \delta\mathbf{S}_{[1]} = \mathbf{S}_{[0]} + k \int \hat{\boldsymbol{\Omega}} \times \mathbf{S}_{[0]} ds, \quad (2.26)$$

where $\delta\mathbf{S}_{[1]}$ means the leading order quantum correction to the *unperturbed* (initial) Stokes vector $\mathbf{S}_{[0]}$. Here the correction can be treated as the leading order perturbation with $\alpha_e/(30\pi)(B/B_c)^2 \sim 10^{-5}(B/B_c)^2$ being a perturbation parameter. Upon inspection of eqs. (2.18) and (2.19) for eq. (2.26), we can further write down our solution in terms of its components:

$$S_1 \approx S_{1[0]} - 2k\eta S_{3[0]} \int B^2 \sin^3 \vartheta \left[(\cos \vartheta + \sin \vartheta) \hat{n}_{y[0]} - \frac{\Omega_p \sin \alpha s}{c(3 \cos^2(\theta - \alpha) + 1)^{1/2}} \right] ds, \quad (2.27)$$

$$S_2 \approx S_{2[0]} + k\eta S_{3[0]} \int B^2 \sin^4 \vartheta ds, \quad (2.28)$$

$$S_3 \approx S_{3[0]} + k\eta \left\{ 2S_{1[0]} \int B^2 \sin^3 \vartheta \left[(\cos \vartheta + \sin \vartheta) \hat{n}_{y[0]} - \frac{\Omega_p \sin \alpha s}{c(3 \cos^2(\theta - \alpha) + 1)^{1/2}} \right] ds - S_{2[0]} \int B^2 \sin^4 \vartheta ds \right\}. \quad (2.29)$$

⁶From eq. (2.5) $B_{\max} = |B(r = r_*, \theta = \alpha)|$.

2.2.1 Examples

We consider X-ray emissions from three neutron stars, (i) one with $B_{\max} \approx 10^{12}$ G and $\Omega_p \approx 392.7$ Hz ($P \approx 0.016$ s), (ii) another with $B_{\max} \approx 5.6 \times 10^{12}$ G and $\Omega_p \approx 22.28$ Hz ($P \approx 0.282$ s), (iii) the third with $B_{\max} \approx 5.0 \times 10^{13}$ G and $\Omega_p \approx 19.6$ Hz ($P \approx 0.32$ s), and assume for all the emissions, $r_o = 2r_* \approx 2 \times 10^6$ cm, $\theta_o = 60^\circ$, $\alpha = 45^\circ$, $\eta \approx 3.97 \times 10^{-32}$ and $\omega \approx 2\pi \times 10^{18}$ Hz ($k \approx 2.0958 \times 10^8$ cm $^{-1}$).⁷ These stars belong to ‘rotation-powered pulsars’ (RPPs) [36].⁸ In figure 2 the three RPPs chosen from the X-ray group are encircled, (i) the one in orange, (ii) another in cyan, (iii) the third in green. Given the X-ray emissions from these, we solve the evolution equations (2.1) for the following cases.

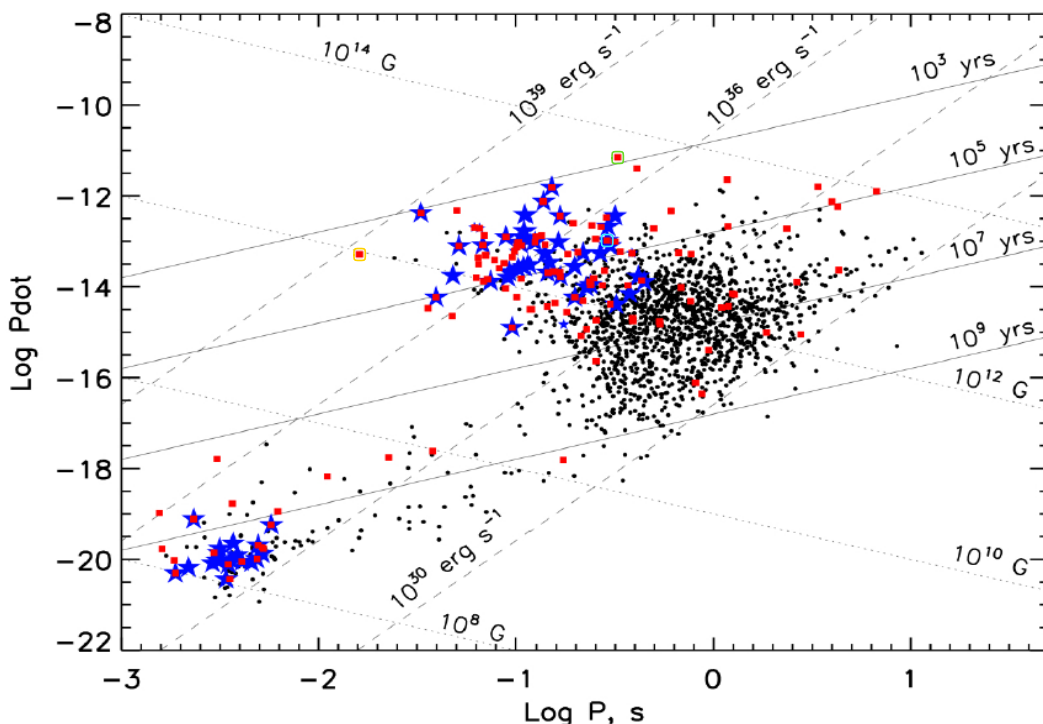


Figure 2: The population of detected rotation-powered pulsars (RPPs) plotted against their rotation period. RPPs detected in X-rays and gamma-rays are represented by red dots and blue stars, respectively. Three RPPs chosen from the X-ray group, (i) one with $B_{\max} \approx 10^{12}$ G and $\Omega_p \approx 392.7$ Hz ($P \approx 0.016$ s), (ii) another with $B_{\max} \approx 5.6 \times 10^{12}$ G and $\Omega_p \approx 22.28$ Hz ($P \approx 0.282$ s), (iii) the third with $B_{\max} \approx 5.0 \times 10^{13}$ G and $\Omega_p \approx 19.6$ Hz ($P \approx 0.32$ s), are encircled in orange, cyan and green colors, respectively. (Credit: [36], reproduced with modifications.)

⁷For the emission location (r_o, θ_o) and the inclination angle α are given the same values for the three stars; the values are not based on actual observations. This is intended for comparing the QED effects from the three different sources under the same conditions.

⁸RPPs refer to neutron stars whose radiation is powered by loss of their rotation energy, via creation and acceleration of e^+e^- pairs in the strong magnetic field, $B_{\max} \sim 10^{11} - 10^{13}$ G. The number of detected RPPs are known to be about ~ 2000 in radio, ~ 10 in optical (including NIR and UV), ~ 100 in X-ray and ~ 100 in gamma-ray emissions [36].

Example (i)

With $B_{\max} \approx 10^{12}$ G and $\Omega_p \approx 392.7$ Hz ($P \approx 0.016$ s), we obtain numerical solutions of eqs. (2.23)-(2.25) (in solid lines) or perturbative solutions by means of eqs. (2.27)-(2.29) (in dashed lines), as shown in figures 3a and 3b, given the initial Stokes vectors $\mathbf{S}(0) = (S_1(0), S_2(0), S_3(0)) = (1, 0, 0)$ and $(0.8, 0, 0.6)$, respectively. The perturbative solutions agree well with numerical ones as $\left|k\hat{\Omega}_{1,2}(s) s\right|_{\max} \sim \left|k\hat{\Omega}_{1,2}(s_{\dagger 1,2}) s_{\dagger 1,2}\right| \sim 10^{-2} \ll 1$, where $s_{\dagger 1,2}$ is the extremum, i.e., $d\hat{\Omega}_{1,2}(s_{\dagger 1,2})/ds = 0$. On the Poincaré sphere, our solutions are represented by the magenta and light blue loci in figure 6a, corresponding to figures 3a and 3b, respectively. The loci imply a fraction of an oscillation for the polarization evolution, as is confirmed later by the approximate analytical solutions in section 2.2.2.

Example (ii)

With $B_{\max} \approx 5.6 \times 10^{12}$ G and $\Omega_p \approx 22.28$ Hz ($P \approx 0.282$ s), we obtain numerical solutions of eqs. (2.23)-(2.25), as shown in figures 4a and 4b, given the initial Stokes vectors $\mathbf{S}(0) = (S_1(0), S_2(0), S_3(0)) = (1, 0, 0)$ and $(0.8, 0, 0.6)$, respectively. On the Poincaré sphere, our solutions are represented by the magenta and light blue loci in figure 6b, corresponding to figures 4a and 4b, respectively. The loci imply about half an oscillation for the polarization evolution, as is confirmed later by the approximate analytical solutions in section 2.2.2.

Example (iii)

With $B_{\max} \approx 5.0 \times 10^{13}$ G and $\Omega_p \approx 19.6$ Hz ($P \approx 0.32$ s), we obtain numerical solutions of eqs. (2.23)-(2.25), as shown in figures 5a and 5b, given the initial Stokes vectors $\mathbf{S}(0) = (S_1(0), S_2(0), S_3(0)) = (1, 0, 0)$ and $(0.8, 0, 0.6)$, respectively. On the Poincaré sphere, our solutions are represented by the magenta and light blue loci in figure 6c, corresponding to figures 5a and 5b, respectively. The loci imply multiple oscillations for the polarization evolution, as is confirmed later by the approximate analytical solutions in section 2.2.2.

2.2.2 Approximate analytical solutions

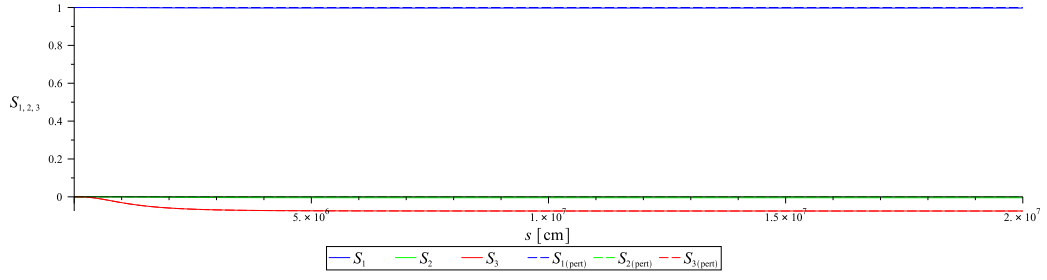
Plotting the birefringent functions $\hat{\Omega}_1(s)$ and $\hat{\Omega}_2(s)$, as given by (2.18) and (2.19), respectively, one can observe that they feature distinctive patterns; they can be well approximated by some analytic models, whose curves resemble the original plots. In figure 7 are plotted the birefringent functions for the three cases: (a) $B_{\max} \approx 10^{12}$ G and $\Omega_p \approx 392.7$ Hz ($P \approx 0.016$ s), (b) $B_{\max} \approx 5.6 \times 10^{12}$ G and $\Omega_p \approx 22.28$ Hz ($P \approx 0.282$ s), (c) $B_{\max} \approx 5.0 \times 10^{13}$ G and $\Omega_p \approx 19.6$ Hz ($P \approx 0.32$ s) with solid lines (see figures 7a, 7b and 7c, respectively), where they have been evaluated with the same initial condition as assumed in section 2.2.1.

In correspondence with the actual birefringent functions above, the following analytical models are also plotted with dashed lines in figure 7:

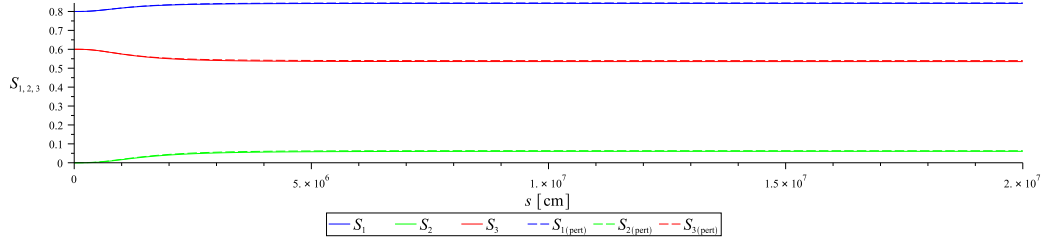
$$\hat{\Omega}_{1,2}(s) \approx -a_{1,2} s^{\frac{p+1}{p}} e^{-bs} \quad \text{for } 0 \leq s \leq 20r_* (\approx 2 \times 10^7 \text{ cm}), \quad (2.30)$$

where $a_1 > 0$, $a_2 < 0$, $b > 0$ and $p > 0$ are free parameters; with suitable values chosen for these, our model functions can give rise to solutions of eqs. (2.23)-(2.25) that match fairly well the numerical results obtained in section 2.2.1. Here we express

$$a_{1,2} = -\hat{\Omega}_{1(\min),2(\max)} \left[\frac{e}{(1-q) s_{\dagger 1} + q s_{\dagger 2}} \right]^{\frac{p+1}{p}}, \quad b = \frac{p+1}{p [(1-q) s_{\dagger 1} + q s_{\dagger 2}]}, \quad (2.31)$$

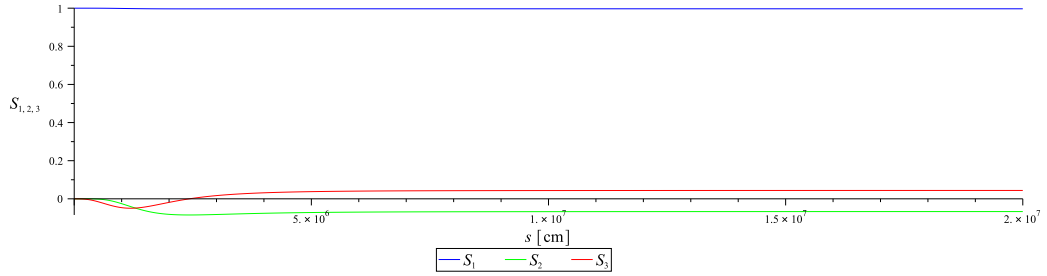


(a) With $\mathbf{S}(0) = (1, 0, 0)$

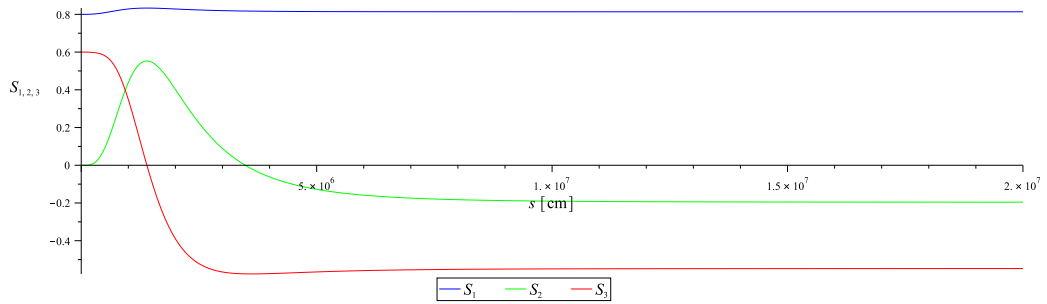


(b) With $\mathbf{S}(0) = (0.8, 0, 0.6)$

Figure 3: For Example (i): the evolution of the Stokes vector $\mathbf{S}(s) = (S_1(s), S_2(s), S_3(s))$, $0 \leq s \leq 20r_*$ ($\approx 2 \times 10^7$ cm), for the X-ray emissions from the pulsar with $B_{\max} \approx 10^{12}$ G and $\Omega_p \approx 392.7$ Hz ($P \approx 0.016$ s).



(a) With $\mathbf{S}(0) = (1, 0, 0)$



(b) With $\mathbf{S}(0) = (0.8, 0, 0.6)$

Figure 4: For Example (ii): the evolution of the Stokes vector $\mathbf{S}(s) = (S_1(s), S_2(s), S_3(s))$, $0 \leq s \leq 20r_*$ ($\approx 2 \times 10^7$ cm), for the X-ray emissions from the pulsar with $B_{\max} \approx 5.6 \times 10^{12}$ G and $\Omega_p \approx 22.28$ Hz ($P \approx 0.282$ s).

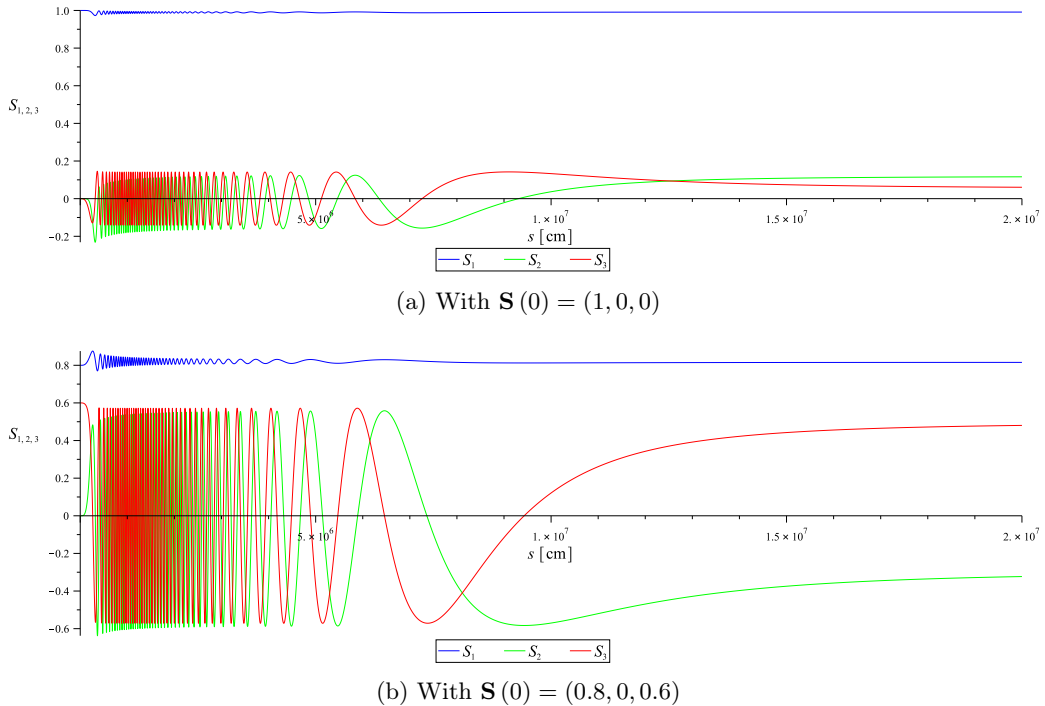


Figure 5: For Example (iii): the evolution of the Stokes vector $\mathbf{S}(s) = (S_1(s), S_2(s), S_3(s))$, $0 \leq s \leq 20r_* (\approx 2 \times 10^7 \text{ cm})$, for the X-ray emissions from the pulsar with $B_{\text{max}} \approx 5.0 \times 10^{13} \text{ G}$ and $\Omega_p \approx 19.6 \text{ Hz}$ ($P \approx 0.32 \text{ s}$).

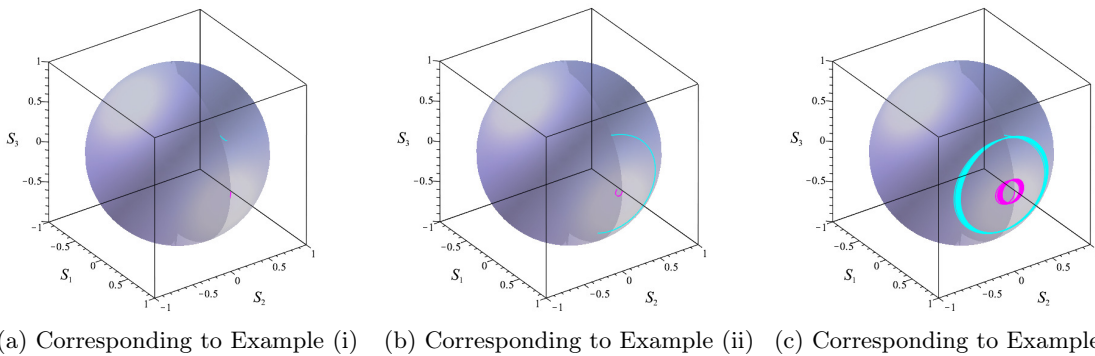


Figure 6: Representations of the Stokes vectors from Examples (i)-(iii) on the Poincaré sphere. The loci imply patterns of the polarization evolution in terms of oscillation.

where $\hat{\Omega}_{1(\text{min}),2(\text{max})} = \hat{\Omega}_{1,2}(s_{\dagger 1,2})$, evaluated from (2.18), (2.19), with $s_{\dagger 1,2}$ denoting the extremum. We have set $p = 100$ (a sufficiently large number) for all three cases, and $q = 0.99999$ for (a) and (b), and $q = 0.0532$ for (c) in figure 7.⁹

Plugging eq. (2.30) into eqs. (2.23)-(2.25), we obtain analytical solutions as follows (for

⁹In particular, the values for q have been chosen such that our solutions converge to the asymptotic limits that match well the numerical results given by figures 3b, 4b and 5b in section 2.2.1, as s tends to ∞ .

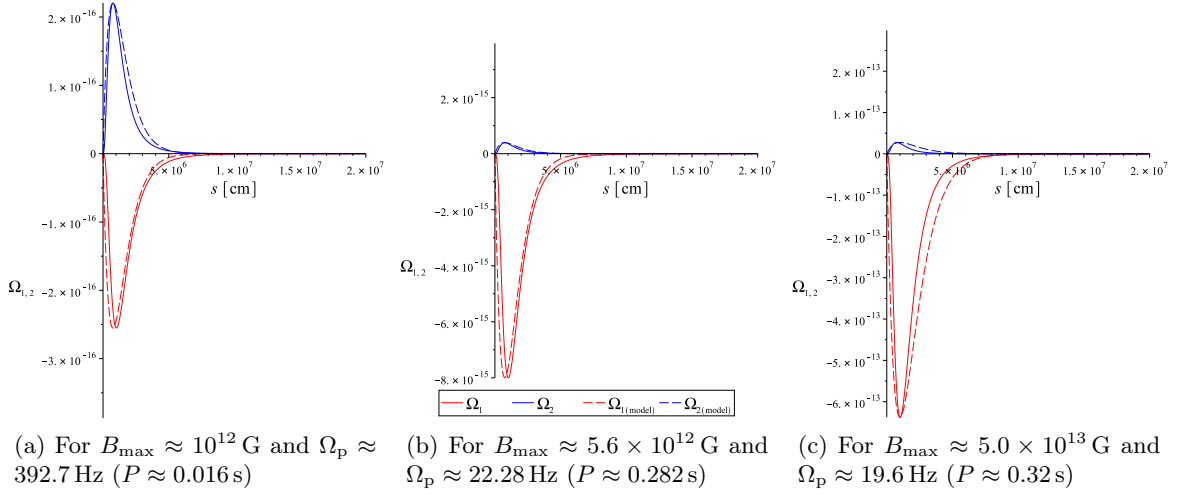


Figure 7: Plots of the birefringent functions $\hat{\Omega}_1(s)$ and $\hat{\Omega}_2(s)$ and their approximate analytic models.

a complete derivation, see Appendix B):

$$S_1(s) \approx \frac{a_2 S_o}{\sqrt{a_1^2 + a_2^2}} \cos(\Psi(s; p) + \delta) + \frac{a_1 C}{\sqrt{a_1^2 + a_2^2}}, \quad (2.32)$$

$$S_2(s) \approx -\frac{a_1 S_o}{\sqrt{a_1^2 + a_2^2}} \cos(\Psi(s; p) + \delta) + \frac{a_2 C}{\sqrt{a_1^2 + a_2^2}}, \quad (2.33)$$

$$S_3(s) \approx S_o \sin(\Psi(s; p) + \delta), \quad (2.34)$$

where

$$\Psi(s; p) \equiv k \sqrt{a_1^2 + a_2^2} b^{-\frac{4p+1}{2p}} s^{\frac{1}{2p}} e^{-\frac{1}{2}bs} \left[M_{\frac{1}{2p}, \frac{p+1}{2p}}(bs) - (bs)^{\frac{2p+1}{2p}} e^{-\frac{1}{2}bs} \right], \quad (2.35)$$

and $M_{\kappa, \mu}(z)$ denotes a Whittaker function of the first kind,¹⁰ and $a_{1,2}$ and b are given by (2.31). Here we determine S_o , C and δ by matching the initial value of the Stokes vector $\mathbf{S}(0) = (S_1(0), S_2(0), S_3(0))$ with eqs. (2.32)-(2.34) evaluated at $s = 0$.

In figure 8 we plot the above solutions (2.32)-(2.34) for the following cases, assuming $r_o = 2r_* \approx 2 \times 10^6$ cm, $\theta_o = 60^\circ$, $\alpha = 45^\circ$, $\eta \approx 3.97 \times 10^{-32}$ for $\hat{\Omega}_{1(\min), 2(\max)} = \hat{\Omega}_{1,2}(s_{\dagger 1, 2})$ (evaluated via (2.18) and (2.19)) and $\omega \approx 2\pi \times 10^{18}$ Hz ($k \approx 2.0958 \times 10^8$ cm $^{-1}$) for the X-ray emissions, with the initial Stokes vector $\mathbf{S}(0) = (0.8, 0, 0.6)$:

Case (a) (see figure 8a);

for $B_{\max} \approx 10^{12}$ G and $\Omega_p \approx 392.7$ Hz ($P \approx 0.016$ s), with the parameters

$\hat{\Omega}_{1(\min)} \approx -2.5511 \times 10^{-16}$, $\hat{\Omega}_{2(\max)} \approx 2.2054 \times 10^{-16}$, $s_{\dagger 1} \approx 1.0202 \times 10^6$ cm, $s_{\dagger 2} \approx 7.5467 \times 10^5$ cm, $p = 100$, $q = 0.99999$ for $a_{1,2}$ and b (evaluated via (2.31)), and $S_o \approx 0.7961$, $C \approx 0.6052$, $\delta \approx 2.2879$,

Case (b) (see figure 8b);

for $B_{\max} \approx 5.6 \times 10^{12}$ G and $\Omega_p \approx 22.28$ Hz ($P \approx 0.282$ s), with the parameters

¹⁰The expression inside the square brackets in eq. (2.35) has been reduced from its original form as given by eq. (B.7) in Appendix B, using the identity $M_{(2p+1)/(2p), (p+1)/(2p)}(bs) = (bs)^{(2p+1)/(2p)} e^{-bs/2} M(0, (2p+1)/p, bs)$, with the Kummer function $M(0, (2p+1)/p, bs) = 1$ as a special case [37].

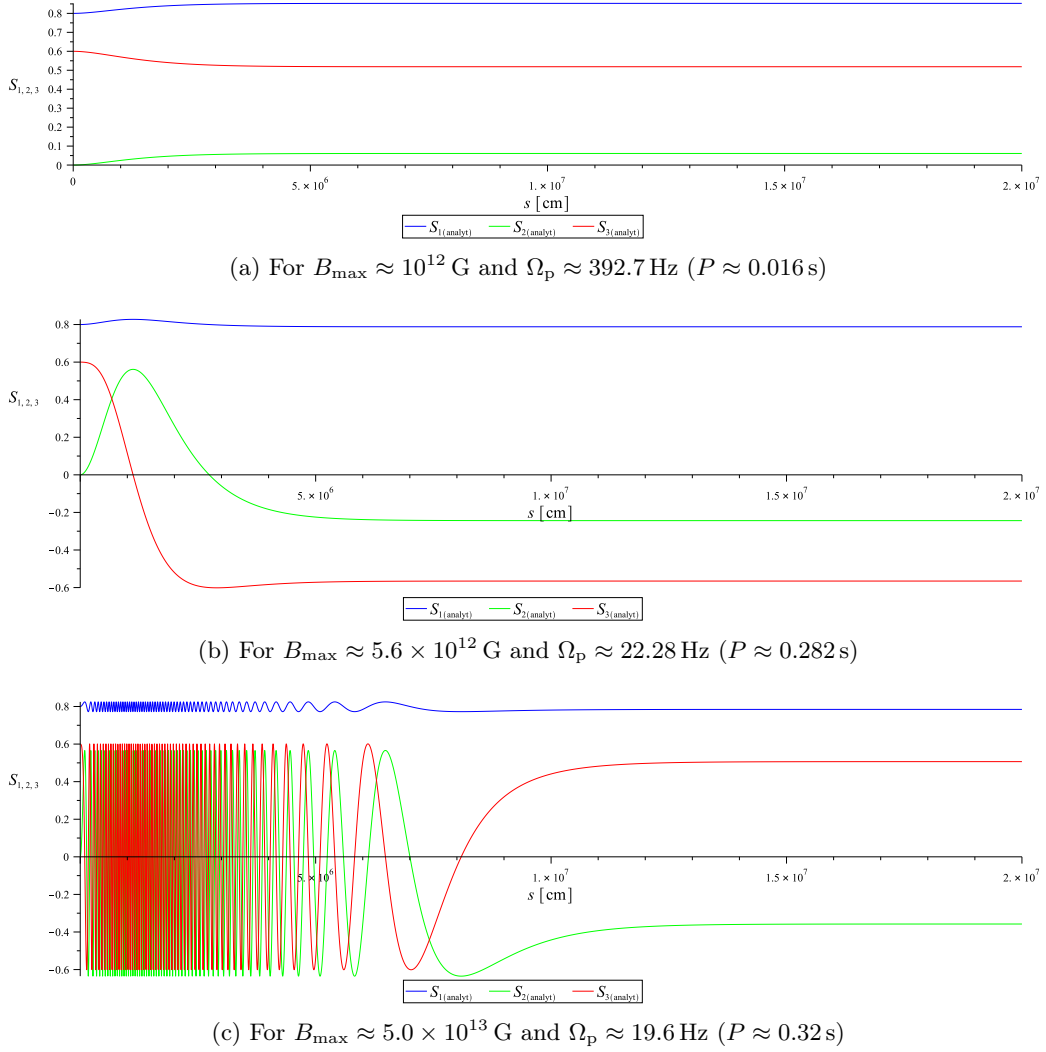


Figure 8: Plots of the analytical solutions $S_1(s)$, $S_2(s)$ and $S_3(s)$, given the initial Stokes vector $\mathbf{S}(0) = (0.8, 0, 0.6)$.

$\hat{\Omega}_{1(\min)} \approx -8.0001 \times 10^{-15}$, $\hat{\Omega}_{2(\max)} \approx 3.9240 \times 10^{-16}$, $s_{\dagger 1} \approx 1.0202 \times 10^6$ cm, $s_{\dagger 2} \approx 7.5467 \times 10^5$ cm, $p = 100$, $q = 0.99999$ for $a_{1,2}$ and b (evaluated via (2.31)), and $S_o \approx 0.6013$, $C \approx 0.7990$, $\delta \approx 1.6360$,

Case (c) (see figure 8c);

for $B_{\max} \approx 5.0 \times 10^{13}$ G and $\Omega_p \approx 19.6$ Hz ($P \approx 0.32$ s), with the parameters $\hat{\Omega}_{1(\min)} \approx -6.3776 \times 10^{-13}$, $\hat{\Omega}_{2(\max)} \approx 2.7567 \times 10^{-14}$, $s_{\dagger 1} \approx 1.0202 \times 10^6$ cm, $s_{\dagger 2} \approx 7.5467 \times 10^5$ cm, $p = 100$, $q = 0.0532$ for $a_{1,2}$ and b (evaluated via (2.31)), and $S_o \approx 0.6010$, $C \approx 0.7993$, $\delta \approx 1.6283$.

These plots compare with figures 3b (for Example (i)), 4b (for Example (ii)) and 5b (for Example (iii)) in section 2.2.1, respectively.

The analytical solutions (2.32)-(2.34) provide a useful tool for understanding the different patterns of polarization evolution for the three cases above, as given by figures 8a, 8b and 8c. Inspecting numerically the functional argument $\Psi(s; p)$ given by (2.35), one can approximate it to a simpler form with the help of (2.30) and (2.31):

For $0 \leq s \lesssim 2.5 \times 10^6$ cm,

$$\begin{aligned} \Psi(s; p = 100) &= k \sqrt{a_1^2 + a_2^2 b^{-\frac{401}{200}} s^{\frac{1}{200}} e^{-\frac{1}{2}bs}} \left[M_{\frac{1}{200}, \frac{101}{200}}(bs) - (bs)^{\frac{201}{200}} e^{-\frac{1}{2}bs} \right] \\ &\approx 0.24k \sqrt{\hat{\Omega}_{1(\min)}^2 + \hat{\Omega}_{2(\max)}^2} \pi s. \end{aligned} \quad (2.36)$$

Using this, we can estimate how much the oscillations for the three cases have progressed, for example, during $0 \leq s \lesssim 2.5 \times 10^6$ cm:

$$\Psi(s \approx 2.5 \times 10^6 \text{ cm}; p = 100) \approx \begin{cases} 0.04\pi & \text{(a fraction of an oscillation) for Case (a),} \\ \pi & \text{(about half an oscillation) for Case (b),} \\ 80\pi & \text{(multiple oscillations) for Case (c),} \end{cases} \quad (2.37)$$

each of which can be checked by comparison with figures 8a, 8b and 8c, respectively.

Recalling Example (i) from section 2.2.1, one finds that the condition for perturbation can be equivalently expressed with the help of (2.36):

$$\begin{aligned} \left| k \hat{\Omega}_{1,2}(s) s \right|_{\max} &\sim \left| k \hat{\Omega}_{1,2}(s_{\dagger 1,2}) s_{\dagger 1,2} \right| \sim 0.24k \sqrt{\hat{\Omega}_{1(\min)}^2 + \hat{\Omega}_{2(\max)}^2} \pi \times 10^6 \text{ cm} \\ &\approx 0.017\pi \ll 1 \text{ for Example (i) or Case (a).} \end{aligned} \quad (2.38)$$

Extending this argument, similarly to (2.37) above we may state the following in reference to the patterns of polarization evolution:

$$\left| k \hat{\Omega}_{1,2}(s) s \right|_{\max} \begin{cases} \ll 1 & \text{(fractionally oscillatory - monotonic) for Example (i),} \\ \sim 1 & \text{(half oscillatory) for Example (ii),} \\ \gg 1 & \text{(highly oscillatory) for Example (iii).} \end{cases} \quad (2.39)$$

These features can also be checked by comparison with the loci on the Poincaré sphere, as given by figures 6a, 6b and 6c, which imply the three different patterns of the polarization evolution in terms of oscillation (by means of the number of turns of the circular loci).

3 Evolution of polarization states in strong magnetic field – quadrupole pulsars

3.1 Modified magnetic field geometry and evolution equations of Stokes vector

The pulsar magnetic field structure may not simply be dipolar as given by (2.5), and one may extend a pulsar model by considering a superposition of dipole and higher-order multipole fields. For example, the simplest superposition would be ‘quadrupole’ fields, composed of dipole and quadrupole fields. The magnetic field of an oblique quadrupole rotator can be written as

$$\begin{aligned} \mathbf{B}_{\text{qd}}(r, \theta, \phi) &= \left[\frac{2\mu_{\text{d}}(\cos \alpha \cos \theta + \sin \alpha \sin \theta \cos \phi)}{r^3} + \frac{\mu_{\text{q}} \left(3(\cos \alpha \cos \theta + \sin \alpha \sin \theta \cos \phi)^2 - 1 \right)}{r^4} \right] \mathbf{e}_{\hat{r}} \\ &+ \left[\frac{\mu_{\text{d}}(\cos \alpha \sin \theta - \sin \alpha \cos \theta \cos \phi)}{r^3} \right. \\ &\quad \left. + \frac{2\mu_{\text{q}}(\cos \alpha \sin \theta - \sin \alpha \cos \theta \cos \phi)(\cos \alpha \cos \theta + \sin \alpha \sin \theta \cos \phi)}{r^4} \right] \mathbf{e}_{\hat{\theta}} \\ &+ \left[\frac{\mu_{\text{d}} \sin \alpha \sin \phi}{r^3} + \frac{2\mu_{\text{q}} \sin \alpha \sin \phi (\cos \alpha \cos \theta + \sin \alpha \sin \theta \cos \phi)}{r^4} \right] \mathbf{e}_{\hat{\phi}}, \end{aligned} \quad (3.1)$$

where the subscript $_{\text{qd}}$ on the left-hand side stands for ‘quadrudipole’ (hereafter, this will be attached to notations for any quantities affected by the quadrudipole field), and μ_{d} and μ_{q} denote the magnetic dipole and quadrupole moments, respectively.

The magnetic dipole moment can be expressed as $\mu_{\text{d}} = \pi r_*^2 I$, as produced by a static loop current I of radius of the neutron star r_* , encircling its equator. Similarly, one can express the magnetic quadrupole moment as $\mu_{\text{q}} = 2\chi\pi r_*^3 I = 2\chi r_* \mu_{\text{d}}$, as produced by two identical magnetic dipole loops carrying opposing equal currents I , each of radius r_* , separated by distance χr_* (i.e., anti-Helmholtz coils), where $\chi > 0$ is a free parameter to determine the ratio between the dipole and quadrupole moments. For example, the magnetic field lines of an oblique quadrudipole rotator, with $\chi = 1$, that is, $\mu_{\text{q}} = 2r_*\mu_{\text{d}}$, set for eq. (3.1) are illustrated in figure 9.

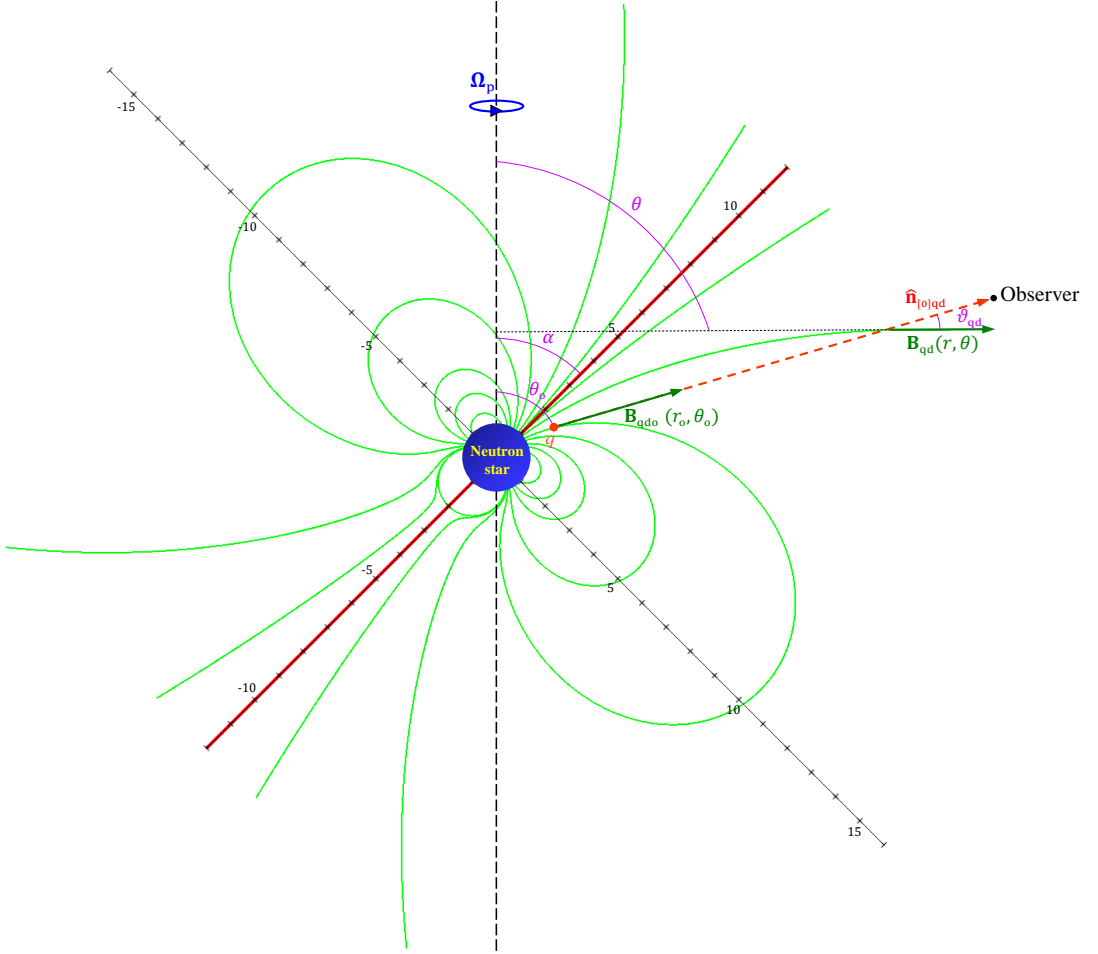


Figure 9: A cross-sectional view of a pulsar magnetosphere with the quadrudipole (dipole + quadrupole) magnetic field lines (green) around a neutron star, where the relation between the magnetic dipole and quadrupole moments is set by $\mu_{\text{q}} = 2r_*\mu_{\text{d}}$ for the total field (3.1). The vertical dashed line (black) and the inclined solid line (red) represent the rotation axis and the magnetic axis, respectively. α between these axes denotes the inclination angle. The scale of the unity in this graph is equivalent to the neutron star radius $\sim 10^6$ cm. The red dashed line represents the trajectory curve of the light ray traced by the propagation vector $\hat{\mathbf{n}}_{[0]\text{qd}}$ as projected onto the xz -plane.

As the magnetic field geometry changes from (2.5) to (3.1), the classical propagation vector shall be modified from (2.6) to

$$\hat{\mathbf{n}}_{[0]\text{qd}} = \beta_{\text{qd}} \hat{\mathbf{B}}_{\text{qd}} + \frac{\boldsymbol{\Omega}_{\text{p}} \times \mathbf{r}}{c}, \quad (3.2)$$

where $\hat{\mathbf{B}}_{\text{qd}} \equiv \mathbf{B}_{\text{qd}}/|\mathbf{B}_{\text{qd}}|$ and

$$\beta_{\text{qd}} \equiv \left[1 - \left(\frac{\Omega_{\text{p}} r}{c} \right)^2 \sin^2 \theta \left(1 - \frac{\sin^2 \alpha \sin^2 \phi}{f(\theta'; \chi)} \right) \right]^{1/2} - \frac{\Omega_{\text{p}} r \sin \alpha \sin \theta \sin \phi}{c [f(\theta'; \chi)]^{1/2}}, \quad (3.3)$$

with

$$f(\theta'; \chi) \equiv 3 \cos^2 \theta' + 1 + 16 \chi \frac{r^*}{r} \cos^3 \theta' + 4 \chi^2 \left(\frac{r^*}{r} \right)^2 (5 \cos^4 \theta' - 2 \cos^2 \theta' + 1) \quad (3.4)$$

and $\cos \theta' \equiv \cos \alpha \cos \theta + \sin \alpha \sin \theta \cos \phi$.

Similarly to section 2.1, taking only the leading order expansions of $\hat{\mathbf{B}}_{\text{qd}}(r_o, \theta_o, \phi)$ and $\beta_{\text{qd}}(r_o, \theta_o, \phi)$ in ϕ from eqs. (3.1) and (3.3), respectively, one can write down the classical propagation vector out of eq. (3.2) in Cartesian coordinates as

$$\hat{\mathbf{n}}_{[0]\text{qd}} = \hat{n}_{x[0]\text{qd}} \mathbf{e}_x + \hat{n}_{y[0]\text{qd}} \mathbf{e}_y + \hat{n}_{z[0]\text{qd}} \mathbf{e}_z \quad (3.5)$$

where

$$\begin{aligned} \hat{n}_{x[0]\text{qd}} \approx & [f(\theta_o - \alpha; \chi)]^{-1/2} \left\{ 2 \cos(\theta_o - \alpha) \sin \theta_o + \sin(\theta_o - \alpha) \cos \theta_o \right. \\ & \left. + 2 \chi \frac{r^*}{r_o} [(3 \cos^2(\theta_o - \alpha) - 1) \sin \theta_o + 2 \cos(\theta_o - \alpha) \sin(\theta_o - \alpha) \cos \theta_o] \right\} \\ & + \mathcal{O}(\phi^2, (\Omega_{\text{p}} r_o / c)^2, \phi(\Omega_{\text{p}} r_o / c)), \end{aligned} \quad (3.6)$$

$$\begin{aligned} \hat{n}_{z[0]\text{qd}} \approx & [f(\theta_o - \alpha; \chi)]^{-1/2} \left\{ 2 \cos(\theta_o - \alpha) \cos \theta_o - \sin(\theta_o - \alpha) \sin \theta_o \right. \\ & \left. + 2 \chi \frac{r^*}{r_o} [(3 \cos^2(\theta_o - \alpha) - 1) \cos \theta_o - 2 \cos(\theta_o - \alpha) \sin(\theta_o - \alpha) \sin \theta_o] \right\} \\ & + \mathcal{O}(\phi^2, (\Omega_{\text{p}} r_o / c)^2, \phi(\Omega_{\text{p}} r_o / c)), \end{aligned} \quad (3.7)$$

and

$$\begin{aligned} \hat{n}_{y[0]\text{qd}} \approx & \frac{\Omega_{\text{p}}}{c} \left\{ [f(\theta_o - \alpha; \chi)]^{-1/2} \sin \alpha \left(1 + 4 \chi \frac{r^*}{r_o} \cos(\theta_o - \alpha) \right) s + r_o \sin \theta_o \right\} \\ & + \mathcal{O}(\phi^2, (\Omega_{\text{p}} r_o / c)^2, \phi(\Omega_{\text{p}} r_o / c)), \end{aligned} \quad (3.8)$$

with $f(\theta_o - \alpha; \chi)$ referring to eq. (3.4) for $\theta = \theta_o$ and $\phi = 0$. In association with $\hat{\mathbf{n}}_{[0]\text{qd}}$, the orthogonal pair of classical mode polarization vectors are determined as

$$\boldsymbol{\varepsilon}_{\text{I}[0]\text{qd}} = \hat{n}_{z[0]\text{qd}} \mathbf{e}_x + \hat{n}_{y[0]\text{qd}} \mathbf{e}_y - \hat{n}_{x[0]\text{qd}} \mathbf{e}_z, \quad (3.9)$$

$$\boldsymbol{\varepsilon}_{\text{II}[0]\text{qd}} = -(\hat{n}_{x[0]\text{qd}} + \hat{n}_{z[0]\text{qd}}) \hat{n}_{y[0]\text{qd}} \mathbf{e}_x + \mathbf{e}_y + (\hat{n}_{x[0]\text{qd}} - \hat{n}_{z[0]\text{qd}}) \hat{n}_{y[0]\text{qd}} \mathbf{e}_z, \quad (3.10)$$

such that the three vectors, $\hat{\mathbf{n}}_{[0]\text{qd}}$, $\boldsymbol{\varepsilon}_{\text{I}[0]\text{qd}}$ and $\boldsymbol{\varepsilon}_{\text{II}[0]\text{qd}}$ form an orthonormal basis.

In addition, due to (3.1) and (3.5), the angle between the photon trajectory and the local magnetic field line, as defined by eq. (2.3) shall be modified. Then we have

$$\begin{aligned} \cos \vartheta_{\text{qd}} &\approx [f(\theta_o - \alpha; \chi)]^{-1/2} [f(\theta - \alpha; \chi)]^{-1/2} \\ &\quad \times [4 \cos(\theta_o - \alpha) \cos(\theta - \alpha) + \sin(\theta_o - \alpha) \sin(\theta - \alpha) + \chi g_1(r, \theta) + \chi^2 g_2(r, \theta)] \\ &\quad + \mathcal{O}\left(\phi^2, (\Omega_p r_o/c)^2, \phi(\Omega_p r_o/c)\right), \end{aligned} \quad (3.11)$$

where

$$\begin{aligned} g_1(r, \theta) &= 4 \frac{r^*}{r_o} [(3 \cos^2(\theta_o - \alpha) - 1) \cos(\theta - \alpha) + \cos(\theta_o - \alpha) \sin(\theta_o - \alpha) \sin(\theta - \alpha)] \\ &\quad + 4 \frac{r^*}{r} [(3 \cos^2(\theta - \alpha) - 1) \cos(\theta_o - \alpha) + \cos(\theta - \alpha) \sin(\theta - \alpha) \sin(\theta_o - \alpha)], \end{aligned} \quad (3.12)$$

$$\begin{aligned} g_2(r, \theta) &= 4 \frac{r^2}{r_o r} [(3 \cos^2(\theta_o - \alpha) - 1)(3 \cos^2(\theta - \alpha) - 1) \\ &\quad + 4 \cos(\theta_o - \alpha) \sin(\theta_o - \alpha) \cos(\theta - \alpha) \sin(\theta - \alpha)]. \end{aligned} \quad (3.13)$$

Now, having \mathbf{B}_{qd} , $\hat{\mathbf{n}}_{[0]\text{qd}}$, $\boldsymbol{\varepsilon}_{\text{I}[0]\text{qd}}$, $\boldsymbol{\varepsilon}_{\text{II}[0]\text{qd}}$ and $\cos \vartheta_{\text{qd}}$ at hand, as given by eqs. (3.1), (3.5), (3.9), (3.10) and (3.11) above, respectively, we modify the evolution equations of the Stokes vector (2.1) to

$$\frac{d\mathbf{S}}{ds} = k \hat{\boldsymbol{\Omega}}_{\text{qd}} \times \mathbf{S}, \quad (3.14)$$

where

$$\hat{\boldsymbol{\Omega}}_{\text{qd}} \equiv \frac{\alpha_e}{30\pi} (B_{\text{qd}}/B_c)^2 \sin^2 \vartheta_{\text{qd}} (\mathcal{E}_{\text{Iqd}}^2 - \mathcal{E}_{\text{IIqd}}^2, 2\mathcal{E}_{\text{Iqd}}\mathcal{E}_{\text{IIqd}}, 0). \quad (3.15)$$

Here $\sin \vartheta_{\text{qd}}$ is defined via (3.11), and

$$\begin{aligned} \mathcal{E}_{\text{Iqd}} &= -\hat{\mathbf{B}}_{\text{qd}} \cdot (\hat{\mathbf{n}}_{[0]\text{qd}} \times \boldsymbol{\varepsilon}_{\text{I}[0]\text{qd}}) \\ &\approx [f(\theta_o - \alpha; \chi)]^{-1/2} [f(\theta - \alpha; \chi)]^{-1/2} \\ &\quad \times \left\{ \left[2 \cos(\theta_o - \alpha) + 2\chi \frac{r^*}{r_o} (3 \cos^2(\theta_o - \alpha) - 1) \right] \left[2 \cos(\theta - \alpha) + 2\chi \frac{r^*}{r} (3 \cos^2(\theta - \alpha) - 1) \right] \right. \\ &\quad \left. + \sin(\theta_o - \alpha) \left[1 + 4\chi \frac{r^*}{r_o} \cos(\theta_o - \alpha) \right] \sin(\theta - \alpha) \left[1 + 4\chi \frac{r^*}{r} \cos(\theta - \alpha) \right] \right\} \hat{n}_{y[0]\text{qd}} \\ &\quad - \mathcal{E}_{\text{IIqd}} \hat{n}_{y[0]\text{qd}} - \frac{\Omega_p \sin \alpha}{c} [f(\theta - \alpha; \chi)]^{-1/2} \left[1 + 4\chi \frac{r^*}{r} \cos(\theta - \alpha) \right] s \\ &\quad + \mathcal{O}\left(\phi^2, (\Omega_p r_o/c)^2, \phi(\Omega_p r_o/c)\right), \end{aligned} \quad (3.16)$$

$$\begin{aligned} \mathcal{E}_{\text{IIqd}} &= -\hat{\mathbf{B}}_{\text{qd}} \cdot (\hat{\mathbf{n}}_{[0]\text{qd}} \times \boldsymbol{\varepsilon}_{\text{II}[0]\text{qd}}) \\ &\approx [f(\theta_o - \alpha; \chi)]^{-1/2} [f(\theta - \alpha; \chi)]^{-1/2} \\ &\quad \times \left\{ \left[2 \cos(\theta - \alpha) + 2\chi \frac{r^*}{r} (3 \cos^2(\theta - \alpha) - 1) \right] \sin(\theta_o - \alpha) \left[1 + 4\chi \frac{r^*}{r_o} \cos(\theta_o - \alpha) \right] \right. \\ &\quad \left. - \left[2 \cos(\theta_o - \alpha) + 2\chi \frac{r^*}{r_o} (3 \cos^2(\theta_o - \alpha) - 1) \right] \sin(\theta - \alpha) \left[1 + 4\chi \frac{r^*}{r} \cos(\theta - \alpha) \right] \right\} \\ &\quad + \mathcal{O}\left(\phi^2, (\Omega_p r_o/c)^2, \phi(\Omega_p r_o/c)\right), \end{aligned} \quad (3.17)$$

with $f(\theta - \alpha; \chi)$ referring to eq. (3.4) for $\phi = 0$.

3.2 Solving the evolution equations

From eq. (3.15) one can write out the non-zero components of the birefringent vector:

$$\hat{\Omega}_{1\text{qd}} \approx -\eta B_{\text{qd}}^2 \sin^2 \vartheta_{\text{qd}} \mathcal{E}_{\text{IIqd}}^2 + \mathcal{O}\left(\phi^2, (\Omega_{\text{p}} r_{\text{o}}/c)^2, \phi(\Omega_{\text{p}} r_{\text{o}}/c)\right), \quad (3.18)$$

$$\hat{\Omega}_{2\text{qd}} \approx 2\eta B_{\text{qd}}^2 \sin^2 \vartheta_{\text{qd}} \mathcal{E}_{\text{Iqd}} \mathcal{E}_{\text{IIqd}} + \mathcal{O}\left(\phi^2, (\Omega_{\text{p}} r_{\text{o}}/c)^2, \phi(\Omega_{\text{p}} r_{\text{o}}/c)\right), \quad (3.19)$$

where $\eta \equiv \alpha_{\text{e}}/(30\pi B_{\text{c}}^2)$, and \mathcal{E}_{Iqd} and $\mathcal{E}_{\text{IIqd}}$ refer to eqs. (3.16) and (3.17), respectively, and $\sin \vartheta_{\text{qd}}$ is defined via eq. (3.11), while

$$B_{\text{qd}} = \frac{B_{\text{max}} r_*^3 [f(\theta - \alpha; \chi)]^{1/2}}{2(1 + 2\chi)(x^2 + z^2)^{3/2}} \quad (3.20)$$

due to eq. (3.1), with B_{max} being the maximum magnetic field intensity at the polar cap, r_* being the neutron star radius and $f(\theta - \alpha; \chi)$ referring to eq. (3.4) for $\phi = 0$. Having eqs. (3.18) and (3.19) at hand, we solve a system of differential equations, i.e., the evolution equations of the Stokes vector, written out in component form from (3.14):

$$\dot{S}_1(s) = k \hat{\Omega}_{2\text{qd}}(s) S_3(s), \quad (3.21)$$

$$\dot{S}_2(s) = -k \hat{\Omega}_{1\text{qd}}(s) S_3(s), \quad (3.22)$$

$$\dot{S}_3(s) = k \left[\hat{\Omega}_{1\text{qd}}(s) S_2(s) - \hat{\Omega}_{2\text{qd}}(s) S_1(s) \right]. \quad (3.23)$$

3.2.1 Examples

We consider again X-ray emissions from the same three RPPs as in section 2.2.1, that is, (i') one with $B_{\text{max}} \approx 10^{12}$ G and $\Omega_{\text{p}} \approx 392.7$ Hz ($P \approx 0.016$ s), (ii') another with $B_{\text{max}} \approx 5.6 \times 10^{12}$ G and $\Omega_{\text{p}} \approx 22.28$ Hz ($P \approx 0.282$ s), (iii') the third with $B_{\text{max}} \approx 5.0 \times 10^{13}$ G and $\Omega_{\text{p}} \approx 19.6$ Hz ($P \approx 0.32$ s), and assume $r_{\text{o}} = 2r_* \approx 2 \times 10^6$ cm, $\theta_{\text{o}} = 60^\circ$, $\alpha = 45^\circ$, $\eta \approx 3.97 \times 10^{-32}$ and $\omega \approx 2\pi \times 10^{18}$ Hz ($k \approx 2.0958 \times 10^8$ cm $^{-1}$) for all three. However, unlike the dipole pulsars as in section 2.2.1, quadrupole pulsars can be modeled by setting the value of an arbitrary parameter χ to determine the ratio between the magnetic dipole and quadrupole moments; we choose two values, $\chi = 1.585$ and 0.85 to model each RPP in our analysis here.¹¹

In figures 10, 11 and 12 are plotted our numerical solutions of eqs. (3.21)-(3.23) for the Stokes vectors in Examples (i'), (ii') and (iii'), respectively. Also, in figure 13 we present the solutions as represented on the Poincaré sphere for $\chi = 1.585$ only; there is little difference in the representations of solutions between $\chi = 1.585$ and 0.85 cases. The solutions represented by the three magenta loci and the three light blue loci in figure 13 correspond to figures 10a, 11a, 12a and figures 10c, 11c, 12c, respectively. In figure 10 for Example (i'), where B_{max} is relatively weak among the three RPPs, general patterns of polarization evolution are shown to be nearly the same for $\chi = 1.585$ and 0.85 , and to be almost the same even to the dipole case as given by figure 3 for Example (i) in section 2.2.1; it is also confirmed by comparing the

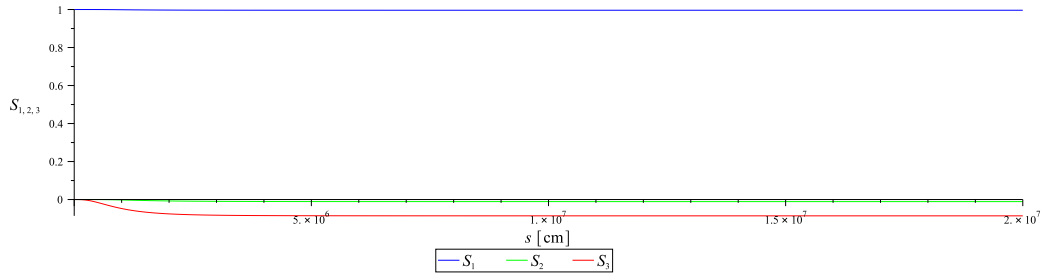
¹¹The values $\chi = 1.585$ and 0.85 have been determined such that they optimize $\hat{\Omega}_{1\text{qd}}(s; \chi) \leq 0$ and $\hat{\Omega}_{2\text{qd}}(s; \chi) \geq 0$, respectively. That is to say, the optimal values of $\hat{\Omega}_{1\text{qd}}(\text{min})$ and $\hat{\Omega}_{2\text{qd}}(\text{max})$ are found at $(s \approx 8.2444 \times 10^5$ cm; $\chi \approx 1.585)$ and $(s \approx 6.3588 \times 10^5$ cm; $\chi \approx 0.85)$, respectively, which are determined from $\partial \hat{\Omega}_{1\text{qd}}(s; \chi)/\partial s = \partial \hat{\Omega}_{1\text{qd}}(s; \chi)/\partial \chi = 0$ and $\partial \hat{\Omega}_{2\text{qd}}(s; \chi)/\partial s = \partial \hat{\Omega}_{2\text{qd}}(s; \chi)/\partial \chi = 0$, respectively. In consideration of eqs. (3.21)-(3.23), these values will maximize the effects of birefringence on our evolution system.

representations in figures 6a and 13a. In contrast, in figure 11 for Example (ii'), where B_{\max} is intermediate among the three RPPs, general patterns of polarization evolution are shown to be nearly the same for $\chi = 1.585$ and 0.85 , but to be noticeably different from the dipole case as given by figure 4 for Example (ii) in section 2.2.1; comparing the representations in figures 6b and 13b, the number of cycles appears to become nearly doubled (from half a cycle to one cycle). However, in figure 12 for Example (iii'), where B_{\max} is the strongest among the three RPPs, general patterns of polarization evolution are shown to be similar for $\chi = 1.585$ and 0.85 , with noticeable differences in phase, but to be significantly different from the dipole case as given by figure 5 for Example (iii) in section 2.2.1; the plots appear to be much denser in the early part of evolution in figure 12 than in figure 5, as the polarization states oscillate much more frequently in the quadrudipole field than in the dipole field, which can also be confirmed by comparing the representations in figures 6c and 13c.

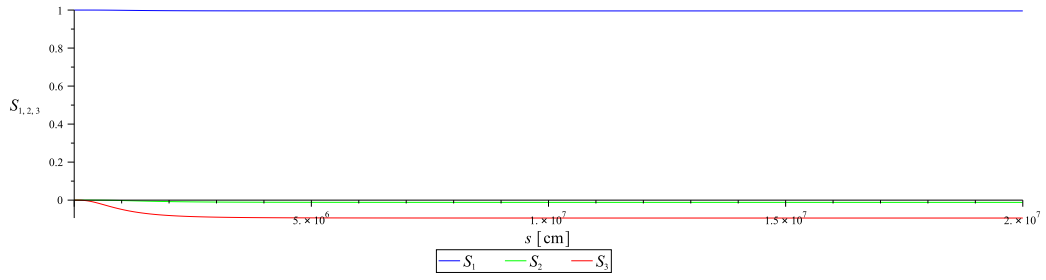
4 Conclusions and discussion

We have investigated the evolution of polarization states of pulsar emission under the quantum refraction effects, combined with the dependence on the emission frequency, for both dipole and quadrudipole pulsar models. To this end, we have solved a system of evolution equations of the Stokes vector given by (2.1) (or by (2.23)-(2.25)) and (3.14) (or by (3.21)-(3.23)) in the dipole and quadrudipole cases, respectively, for three examples of RPPs at a fixed frequency for specific emissions (e.g., X-rays as in sections 2.2.1, 2.2.2 and 3.2.1). Our main results are presented by figures 3-5 and 10-12 in the dipole and quadrudipole cases, respectively, from numerical solutions and in part from perturbative solutions. Also, we have replaced the birefringent vector with some approximate models as in figure 7 to solve the evolution equations analytically in the dipole case, and obtained the results as presented by figure 8, from approximate analytical solutions. It is noteworthy that at a fixed frequency of emission the evolution of the Stokes vector largely exhibits three different patterns, depending on the magnitudes of the birefringent vector, in which the magnetic field strength is a dominant factor: (i) fractionally oscillatory - monotonic, or (ii) half-oscillatory, or (iii) highly oscillatory behaviors. These features are shown by the numerical solutions in figures 3-6, and also confirmed by the approximate analytical solutions in figure 8. In addition, we have examined how the aforementioned features change in the quadrudipole case.

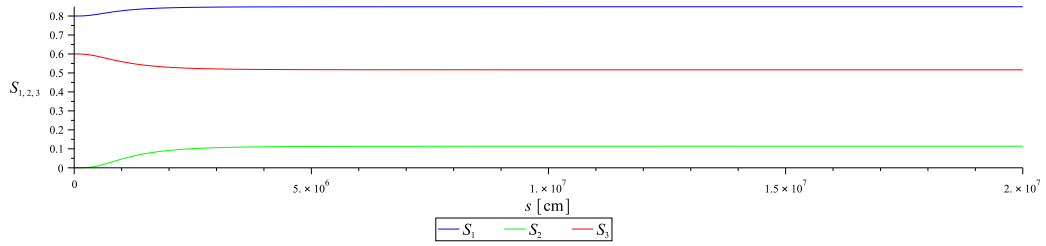
This study is centered on solving the evolution equations for polarization states (2.1), wherein the birefringent vector that contains all information about the quantum refraction effects, coupled to the frequency of pulsar emission, acts on the Stokes vector; the evolution results from the combination of the quantum refraction effects and the frequency dependence of the emission. This is a major difference from our previous work [20], wherein the same effects are independent of the emission frequency; the work solely focuses on the quantum refraction effects on the propagation and polarization of a photon from pulsar emission, with no reference to other properties of the emission, such as the frequency. In this regard, it is worthwhile to draw comparison between the two quantities, the polarization vector and the Stokes vector, both of which are used to describe polarization states. The polarization vector is defined directly from the radiative electric field vector (i.e., the unit electric field vector), and it is parallel-transported along the the propagation vector; usually, we consider such two vectors orthogonal to each other and to the propagation vector to define an orthonormal basis consisting of the three vectors. In contrast, the Stokes vector is defined from Stokes parameters which are built out of the radiative electric field vector [38]. The representation



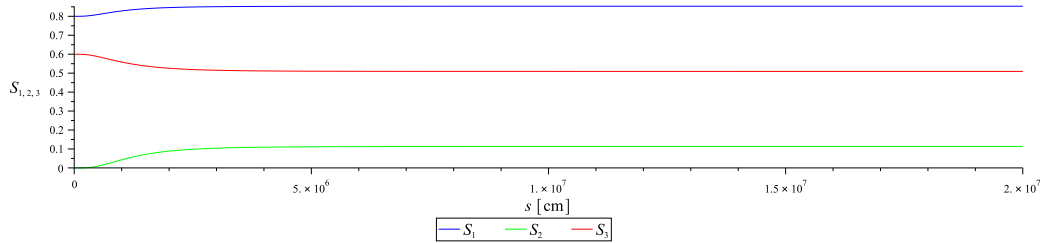
(a) With $\mathbf{S}(0) = (1, 0, 0)$ and $\chi = 1.585$



(b) With $\mathbf{S}(0) = (1, 0, 0)$ and $\chi = 0.85$



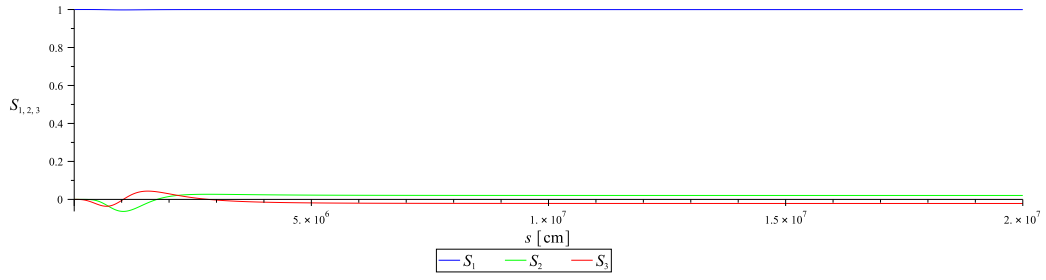
(c) With $\mathbf{S}(0) = (0.8, 0, 0.6)$ and $\chi = 1.585$



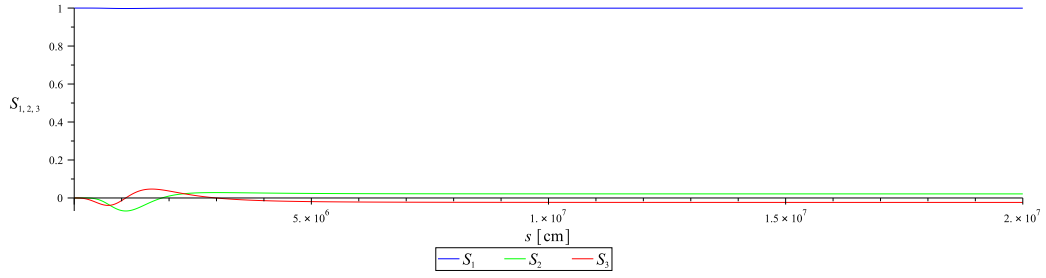
(d) With $\mathbf{S}(0) = (0.8, 0, 0.6)$ and $\chi = 0.85$

Figure 10: For Example (i'): the evolution of the Stokes vector $\mathbf{S}(s) = (S_1(s), S_2(s), S_3(s))$, $0 \leq s \leq 20r_*$ ($\approx 2 \times 10^7$ cm), for the X-ray emissions from the quadrupole pulsar with $B_{\max} \approx 10^{12}$ G and $\Omega_p \approx 392.7$ Hz ($P \approx 0.016$ s).

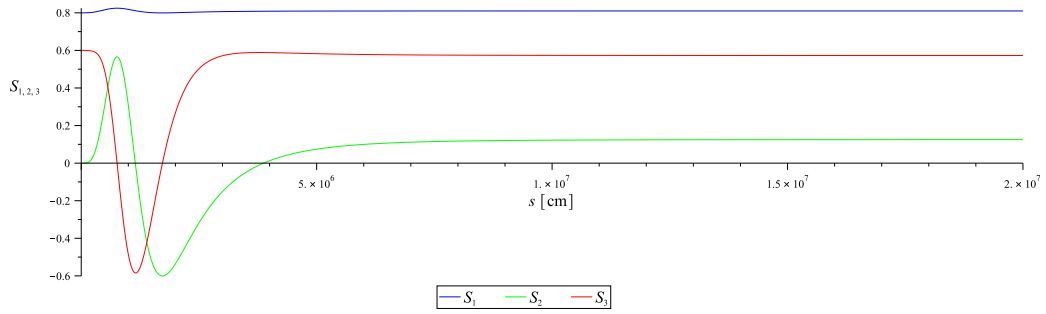
of the Stokes vector is abstract in the sense that it is a vector defined on the Poincaré sphere. The Stokes vector is not parallel-transported along the the propagation vector, but can still be defined along the propagation vector as the two polarization vectors move along it; hence, it can be parameterized by s to represent polarization states along the photon trajectory. However, the Stokes vector has a crucial advantage over the polarization vector in representing polarization states in some astrophysical studies like this: it can be directly



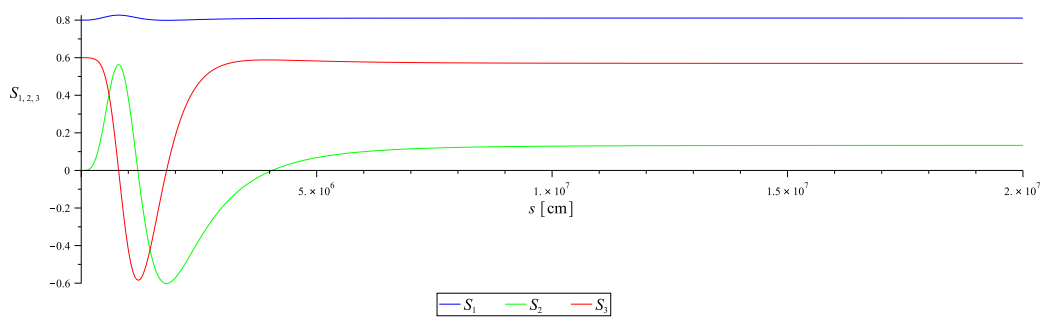
(a) With $\mathbf{S}(0) = (1, 0, 0)$ and $\chi = 1.585$



(b) With $\mathbf{S}(0) = (1, 0, 0)$ and $\chi = 0.85$



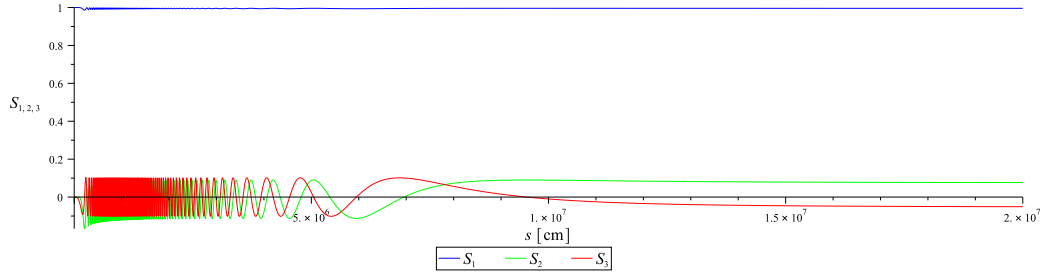
(c) With $\mathbf{S}(0) = (0.8, 0, 0.6)$ and $\chi = 1.585$



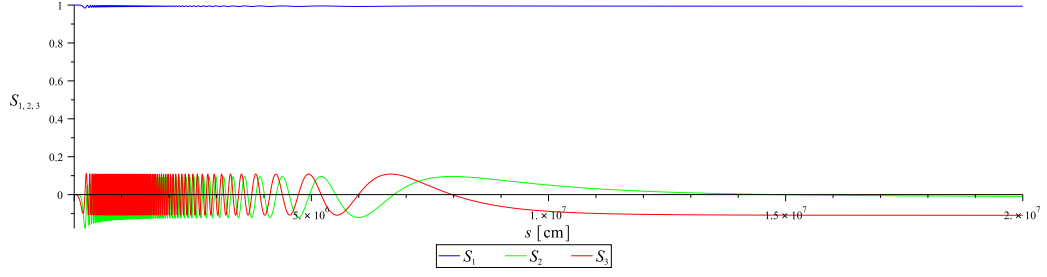
(d) With $\mathbf{S}(0) = (0.8, 0, 0.6)$ and $\chi = 0.85$

Figure 11: For Example (ii'): the evolution of the Stokes vector $\mathbf{S}(s) = (S_1(s), S_2(s), S_3(s))$, $0 \leq s \leq 20r_*$ ($\approx 2 \times 10^7$ cm), for the X-ray emissions from the quadrupole pulsar with $B_{\max} \approx 5.6 \times 10^{12}$ G and $\Omega_p \approx 22.28$ Hz ($P \approx 0.282$ s).

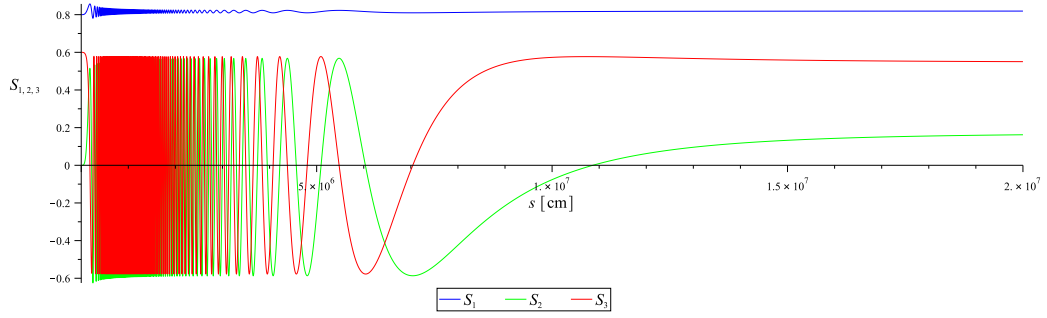
estimated from polarimetric measurements and accommodate depolarization effects due to incomplete coherence and random processes during the photon propagation [39].



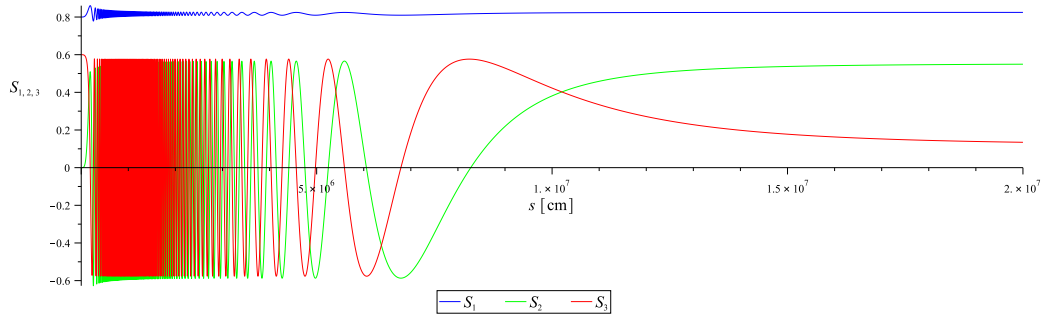
(a) With $\mathbf{S}(0) = (1, 0, 0)$ and $\chi = 1.585$



(b) With $\mathbf{S}(0) = (1, 0, 0)$ and $\chi = 0.85$



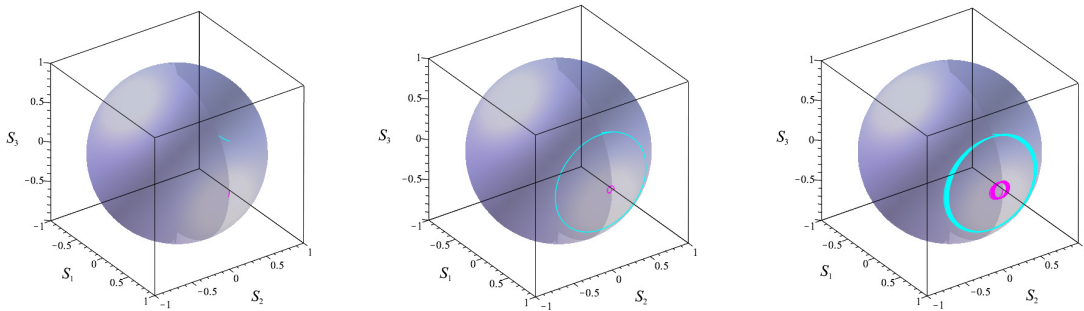
(c) With $\mathbf{S}(0) = (0.8, 0, 0.6)$ and $\chi = 1.585$



(d) With $\mathbf{S}(0) = (0.8, 0, 0.6)$ and $\chi = 0.85$

Figure 12: For Example (iii)': the evolution of the Stokes vector $\mathbf{S}(s) = (S_1(s), S_2(s), S_3(s))$, $0 \leq s \leq 20r_* (\approx 2 \times 10^7 \text{ cm})$, for the X-ray emissions from the quadrupole pulsar with $B_{\text{max}} \approx 5.0 \times 10^{13} \text{ G}$ and $\Omega_p \approx 19.6 \text{ Hz}$ ($P \approx 0.32 \text{ s}$).

With regard to the adiabatic evolution condition as mentioned in [25, 30, 31], we have carefully examined our results presented in figures 3-5 to see what interpretations the condition



(a) Corresponding to Example (i') (b) Corresponding to Example (ii') (c) Corresponding to Example (iii')

Figure 13: Representations of the Stokes vectors from Examples (i')-(iii') for $\chi = 1.585$ on the Poincaré sphere. The loci imply patterns of the polarization evolution in terms of oscillation.

leads to. Solving the condition $\left| k\hat{\Omega} \left(d \ln |k\hat{\Omega}| / ds \right)^{-1} \right| \gtrsim 0.05$ for s (note that our $k\hat{\Omega}$ is equivalent to the birefringent vector as defined in the references above and that we have set the condition value to 0.05 rather than 0.5 as in the references) yields $s_{PL1} \lesssim s \lesssim s_{PL2}$, where $s_{PL1[2]}$ refers to the lower [upper] bound for the ‘polarization limiting’ distance as measured from the emission point. Using this, we have checked out the following: (1) for $6.2 \times 10^5 \text{ cm} \lesssim s \lesssim 1.8 \times 10^6 \text{ cm}$ in figure 3, (2) for $3.1 \times 10^5 \text{ cm} \lesssim s \lesssim 6.2 \times 10^6 \text{ cm}$ in figure 4, (3) for $1.1 \times 10^5 \text{ cm} \lesssim s \lesssim 1.9 \times 10^7 \text{ cm}$ in figure 5, our Stokes vector evolves evidently; otherwise, it freezes.

Effects of gravitation have not been considered in this study. However, close to the neutron star, where gravitation due to the neutron star mass may not be negligible, its effects must be taken into account in our analysis. Then, basically, the following shall be redefined in curved spacetime: (1) the QED one-loop effective Lagrangian, (2) the refractive index for the photon propagation, (3) the magnetic field geometry in the magnetosphere, (4) the radiative electric field due to a charge moving along a magnetic field line, (5) the photon trajectory. All these have not been rigorously dealt with in previous studies. In this regard, inclusion of the gravitational effects will involve non-trivial and immense analyses, and therefore shall be conducted for a long-term plan in our future studies.

A The classical Stokes vector

Consider a particle with a charge q moving along a curved trajectory (a magnetic field line). Then the curvature radiation due to this can be expressed by the electric field:

$$\mathbf{E}(t) = \frac{q}{c|\mathbf{r} - \boldsymbol{\xi}(t_{\text{ret}})|} \frac{\mathbf{n} \times \left[\left(\mathbf{n} - \frac{\dot{\boldsymbol{\xi}}(t_{\text{ret}})}{c} \right) \times \frac{\ddot{\boldsymbol{\xi}}(t_{\text{ret}})}{c} \right]}{\left(1 - \frac{\dot{\boldsymbol{\xi}}(t_{\text{ret}})}{c} \cdot \mathbf{n} \right)^3}, \quad (\text{A.1})$$

where $t_{\text{ret}} \equiv t - r/c$ is the retarded time, $\boldsymbol{\xi}$ represents the particle’s trajectory, \mathbf{n} is the propagation direction of the radiation, and an over-dot ‘ denotes differentiation with respect to t . In a suitably chosen Cartesian frame, by setting $\boldsymbol{\xi}(t_{\text{ret}}) = \rho (\sin(\beta c t_{\text{ret}}/\rho), 0, \cos(\beta c t_{\text{ret}}/\rho))$, with ρ being the radius of curvature of the particle’s trajectory, and $\mathbf{n} = (\cos \varphi, \sin \varphi, 0)$,

with φ being the angle measured from the x -axis to the plane of the particle's motion, we can construct a simple toy model for pulse profiles of pulsar curvature emission as described below [33].

One can express Stokes parameters out of the radiation field (A.1), which describe polarization properties of the curvature radiation [40]:

$$\begin{aligned} I &= \tilde{E}_{\parallel}^* \tilde{E}_{\parallel} + \tilde{E}_{\perp}^* \tilde{E}_{\perp} \\ &= \mathcal{E}_o^2 \omega^2 \left[(\delta^2 + \varphi^2)^2 \text{K}_{2/3}^2 \left(\frac{\rho\omega}{3\beta c} (\delta^2 + \varphi^2)^{3/2} \right) + \varphi^2 (\delta^2 + \varphi^2) \text{K}_{1/3}^2 \left(\frac{\rho\omega}{3\beta c} (\delta^2 + \varphi^2)^{3/2} \right) \right], \end{aligned} \quad (\text{A.2})$$

$$\begin{aligned} Q &= \tilde{E}_{\parallel}^* \tilde{E}_{\parallel} - \tilde{E}_{\perp}^* \tilde{E}_{\perp} \\ &= \mathcal{E}_o^2 \omega^2 \left[(\delta^2 + \varphi^2)^2 \text{K}_{2/3}^2 \left(\frac{\rho\omega}{3\beta c} (\delta^2 + \varphi^2)^{3/2} \right) - \varphi^2 (\delta^2 + \varphi^2) \text{K}_{1/3}^2 \left(\frac{\rho\omega}{3\beta c} (\delta^2 + \varphi^2)^{3/2} \right) \right], \end{aligned} \quad (\text{A.3})$$

$$U = \tilde{E}_{\parallel}^* \tilde{E}_{\perp} + \tilde{E}_{\parallel} \tilde{E}_{\perp}^* = 0, \quad (\text{A.4})$$

$$\begin{aligned} V &= -i \left(\tilde{E}_{\parallel}^* \tilde{E}_{\perp} - \tilde{E}_{\parallel} \tilde{E}_{\perp}^* \right) \\ &= -2\mathcal{E}_o^2 \omega^2 \varphi (\delta^2 + \varphi^2)^{3/2} \text{K}_{2/3} \left(\frac{\rho\omega}{3\beta c} (\delta^2 + \varphi^2)^{3/2} \right) \text{K}_{1/3} \left(\frac{\rho\omega}{3\beta c} (\delta^2 + \varphi^2)^{3/2} \right), \end{aligned} \quad (\text{A.5})$$

where \tilde{E}_{\parallel} and \tilde{E}_{\perp} denote the components of the Fourier transform $\tilde{\mathbf{E}}(\omega) = \tilde{E}_{\parallel}(\omega) \mathbf{e}_z + \tilde{E}_{\perp}(\omega) \mathbf{e}_y = \int_{-\infty}^{\infty} \mathbf{E}(t) \exp(i\omega t) dt$, expressed in the Cartesian frame, and $*$ means the complex conjugate, and $\mathcal{E}_o = q\beta / (2\sqrt{3}\pi^2 r\rho)$, and $\delta \equiv \gamma^{-1} = (1 - \beta^2)^{1/2} \ll 1$ is the half-angle of the beam emission, and $\text{K}_{1/3}$ and $\text{K}_{2/3}$ denote the modified Bessel functions of the second kind. With regard to the polarization state of the curvature radiation, I is a measure of the total intensity, Q and U jointly describe the linear polarization, and V describes the circular polarization. These parameters can be plotted as functions of the phase angle φ , where $\varphi \leq \delta \ll 5^\circ$ usually, to simulate the pulse profiles of pulsar emission theoretically.

Out of the Stokes parameters, one can define the Stokes vector $\mathbf{S} = (S_1, S_2, S_3) \equiv (Q/I, U/I, V/I)$ and express it using (A.2)-(A.5):

$$S_1 = \frac{(\delta^2 + \varphi^2) \text{K}_{2/3}^2 \left(\frac{\rho\omega}{3\beta c} (\delta^2 + \varphi^2)^{3/2} \right) - \varphi^2 \text{K}_{1/3}^2 \left(\frac{\rho\omega}{3\beta c} (\delta^2 + \varphi^2)^{3/2} \right)}{(\delta^2 + \varphi^2) \text{K}_{2/3}^2 \left(\frac{\rho\omega}{3\beta c} (\delta^2 + \varphi^2)^{3/2} \right) + \varphi^2 \text{K}_{1/3}^2 \left(\frac{\rho\omega}{3\beta c} (\delta^2 + \varphi^2)^{3/2} \right)}, \quad (\text{A.6})$$

$$S_2 = 0, \quad (\text{A.7})$$

$$S_3 = -\frac{2\varphi (\delta^2 + \varphi^2)^{1/2} \text{K}_{2/3} \left(\frac{\rho\omega}{3\beta c} (\delta^2 + \varphi^2)^{3/2} \right) \text{K}_{1/3} \left(\frac{\rho\omega}{3\beta c} (\delta^2 + \varphi^2)^{3/2} \right)}{(\delta^2 + \varphi^2) \text{K}_{2/3}^2 \left(\frac{\rho\omega}{3\beta c} (\delta^2 + \varphi^2)^{3/2} \right) + \varphi^2 \text{K}_{1/3}^2 \left(\frac{\rho\omega}{3\beta c} (\delta^2 + \varphi^2)^{3/2} \right)}. \quad (\text{A.8})$$

In figure 14 is plotted the classical Stokes vector against the phase angle φ , where we have set, for example, $\delta \approx 10^{-8}$, $\rho \approx 10^8$ cm, $\beta \approx 1$ and $\omega \approx 2\pi \times 10^{18}$ Hz to model pulse profiles of X-ray pulsar emission. Here the initial values for the Stokes vector, $\mathbf{S}(\varphi = 0) = (1, 0, 0)$ and $\mathbf{S}(\varphi \approx -1.16 \times 10^{-6} \text{ rad}) = (0.8, 0, 0.6)$, as in the examples given in section 2.2.1, are marked by solid circles and solid boxes, respectively.

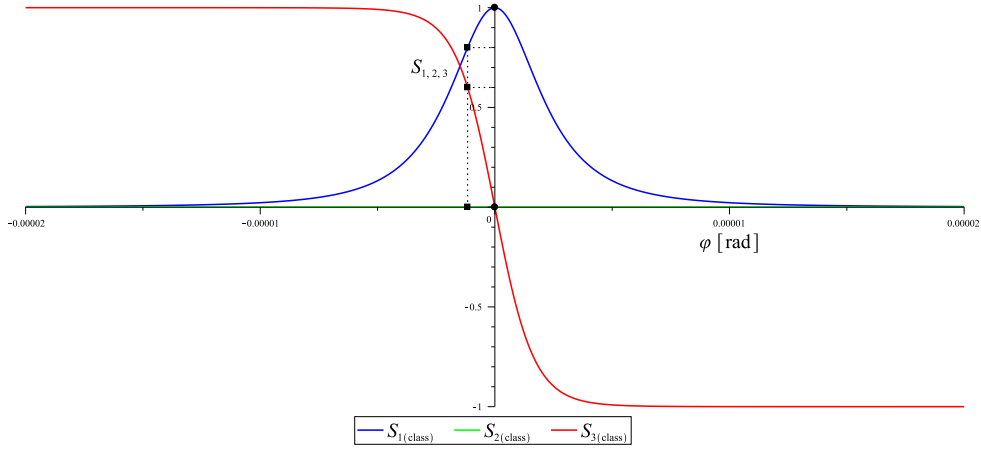


Figure 14: The classical Stokes vector $\mathbf{S}(\varphi) = (S_1(\varphi), S_2(\varphi), S_3(\varphi))$ plotted against the phase angle φ . Its initial values $\mathbf{S}(\varphi = 0) = (1, 0, 0)$ and $\mathbf{S}(\varphi \approx -1.16 \times 10^{-6} \text{ rad}) = (0.8, 0, 0.6)$ are marked by solid circles and solid boxes, respectively.

B Approximate analytical solutions to evolution equations

Substituting eq. (2.30) into eqs. (2.23)-(2.25), the evolution equations can be reduced as follows:

For $0 \leq s \leq 20r_*$,

$$\dot{S}_1(s) \approx -ka_2 s^{\frac{p+1}{p}} e^{-bs} S_3(s), \quad (\text{B.1})$$

$$\dot{S}_2(s) \approx ka_1 s^{\frac{p+1}{p}} e^{-bs} S_3(s), \quad (\text{B.2})$$

$$\ddot{S}_3(s) - \left(\frac{p+1}{ps} - b \right) \dot{S}_3(s) + k^2 (a_1^2 + a_2^2) \left(s^{\frac{p+1}{p}} e^{-bs} \right)^2 S_3(s) \approx 0. \quad (\text{B.3})$$

First, we solve eq. (B.3) for $S_3(s)$, and then using this solution, obtain $S_1(s)$ and $S_2(s)$, by integrating eqs. (B.1) and (B.2), respectively:

$$S_3(s) \approx S_o \sin(\Psi(s; p) + \delta), \quad (\text{B.4})$$

$$S_1(s) \approx \frac{a_2 S_o}{\sqrt{a_1^2 + a_2^2}} \cos(\Psi(s; p) + \delta) + S_{1o}, \quad (\text{B.5})$$

$$S_2(s) \approx -\frac{a_1 S_o}{\sqrt{a_1^2 + a_2^2}} \cos(\Psi(s; p) + \delta) + S_{2o}, \quad (\text{B.6})$$

where

$$\Psi(s; p) \equiv k \sqrt{a_1^2 + a_2^2} b^{-\frac{4p+1}{2p}} s^{\frac{1}{2p}} e^{-\frac{1}{2}bs} \left[M_{\frac{1}{2p}, \frac{p+1}{2p}}(bs) - M_{\frac{2p+1}{2p}, \frac{p+1}{2p}}(bs) \right], \quad (\text{B.7})$$

and $M_{\kappa, \mu}(z)$ denotes a Whittaker function of the first kind. Here employing the identity $S_1^2(s) + S_2^2(s) + S_3^2(s) = 1$ (conservation of the degree of polarization), one can specify S_{1o} and S_{2o} in terms of a_1 , a_2 and a constant C , and establish a relation between S_o and C :

$$S_{1o} = \frac{Ca_1}{\sqrt{a_1^2 + a_2^2}}, \quad S_{2o} = \frac{Ca_2}{\sqrt{a_1^2 + a_2^2}}, \quad S_o^2 + C^2 = 1. \quad (\text{B.8})$$

Then S_o , C and δ are determined by matching the initial value of the Stokes vector $\mathbf{S}(0) = (S_1(0), S_2(0), S_3(0))$ with eqs. (B.4)-(B.6) evaluated at $s = 0$.

Acknowledgments

D.-H.K was supported by the Basic Science Research Program through the National Research Foundation of Korea (NRF) funded by the Ministry of Education (NRF-2021R1I1A1A01054781). C.M.K. was supported by Ultrashort Quantum Beam Facility operation program (140011) through APRI, GIST and GIST Research Institute (GRI) grant funded by GIST. S.P.K. was also in part supported by National Research Foundation of Korea (NRF) funded by the Ministry of Education (NRF-2019R1I1A3A01063183).

References

- [1] W. Heisenberg and H. Euler, *Folgerungen aus der Diracschen Theorie des Positrons*, *Zeitschr. Phys* **98** (1936) 714.
- [2] J. Schwinger, *On Gauge Invariance and Vacuum Polarization*, *Phys. Rev.* **82** (1951) 664.
- [3] P. Meszaros, *High-energy radiation from magnetized neutron stars*, The University Of Chicago Press, Chicago (1992).
- [4] R. Ruffini, G. Vereshchagin and S.-S. Xue, *Electron–positron pairs in physics and astrophysics: from heavy nuclei to black holes*, *Phys. Rept.* **487** (2010) 1.
- [5] A. Fedotov, A. Ilderton, F. Karbstein, B. King, D. Seipt, H. Taya et al., *Advances in QED with intense background fields*, *Phys. Rept.* **1010** (2023) 1 [2203.00019].
- [6] K. Hattori, K. Itakura and S. Ozaki, *Strong-field physics in QED and QCD: From fundamentals to applications*, *Prog. Part. Nucl. Phys.* **133** (2023) 104068 [2305.03865].
- [7] A. Ejlli, F. Della Valle, U. Gastaldi, G. Messineo, R. Pengo, G. Ruoso et al., *The PVLAS experiment: A 25 year effort to measure vacuum magnetic birefringence*, *Phys. Rept.* **871** (2020) 1 [2005.12913].
- [8] F. Karbstein, C. Sundqvist, K.S. Schulze, I. Uschmann, H. Gies and G.G. Paulus, *Vacuum birefringence at x-ray free-electron lasers*, *New J. Phys.* **23** (2021) 095001.
- [9] B. Shen, Z. Bu, J. Xu, T. Xu, L. Ji, R. Li et al., *Exploring vacuum birefringence based on a 100 PW laser and an x-ray free electron laser beam*, *Plasma Phys. Control. Fusion* **60** (2018) 044002.
- [10] Q. Yu, D. Xu, B. Shen, T.E. Cowan and H.-P. Schlenvoigt, *X-ray polarimetry and its application to strong-field quantum electrodynamics*, *High Power Laser Sci. Eng.* **11** (2023) e71.
- [11] C.N. Danson, C. Haefner, J. Bromage, T. Butcher, J.-C.F. Chanteloup, E.A. Chowdhury et al., *Petawatt and exawatt class lasers worldwide*, *High Power Laser Sci. Eng.* **7** (2019) e54.
- [12] A.K. Harding and D. Lai, *Physics of strongly magnetized neutron stars*, *Rep. Prog. Phys.* **69** (2006) 2631.
- [13] R. Taverna et al., *Polarized x-rays from a magnetar*, *Science* **378** (2022) 646.
- [14] A. Santangelo, S. Zane, H. Feng, R. Xu, V. Doroshenko, E. Bozzo et al., *Physics and astrophysics of strong magnetic field systems with eXTP*, *Sci China-Phys Mech Astron* **62** (2019) 1.
- [15] Z. Wadiasingh, G. Younes, M.G. Baring, A.K. Harding, P.L. Gonthier, K. Hu et al., *Magnetars as Astrophysical Laboratories of Extreme Quantum Electrodynamics: The Case for a Compton Telescope*, *Bull. Am. Astron. Soc.* **51** (2019) .
- [16] G.G. Raffelt, *Stars as laboratories for fundamental physics: the astrophysics of neutrinos, axions, and other weakly interacting particles*, The University Of Chicago Press, Chicago (1996).

- [17] S.L. Adler, *Photon splitting and photon dispersion in a strong magnetic field*, *Ann. Phys.* **67** (1971) 599.
- [18] W.-T. Ni, H.-H. Mei and S.-J. Wu, *Foundations of classical electrodynamics, equivalence principle and cosmic interactions: A short exposition and an update*, *Mod. Phys. Lett. A* **28** (2013) 1340013.
- [19] V.I. Denisov, B.N. Shvilkin, V.A. Sokolov and M.I. Vasili'ev, *Pulsar radiation in post-maxwellian vacuum nonlinear electrodynamics*, *Phys. Rev. D* **94** (2016) 045021.
- [20] D.-H. Kim, C.M. Kim and S.P. Kim, *Quantum refraction effects in pulsar emission*, *Monthly Notices of the Royal Astronomical Society* **531** (2024) 2148 [<https://academic.oup.com/mnras/article-pdf/531/1/2148/57953230/stae1304.pdf>].
- [21] S.E. Gralla, A. Lupasca and A. Philippov, *Pulsar magnetospheres: Beyond the flat spacetime dipole*, *The Astrophysical Journal* **833** (2016) 258.
- [22] W. Lockhart, S.E. Gralla, F. Özel and D. Psaltis, *X-ray light curves from realistic polar cap models: inclined pulsar magnetospheres and multipole fields*, *Monthly Notices of the Royal Astronomical Society* **490** (2019) 1774 [<https://academic.oup.com/mnras/article-pdf/490/2/1774/30194725/stz2524.pdf>].
- [23] J. Kazmierczak, "NASA's NICER Delivers Best-ever Pulsar Measurements, 1st Surface Map." <https://www.nasa.gov/universe/nasas-nicer-delivers-best-ever-pulsar-measurements-1st-surface-map/>, 2019.
- [24] C. Kalapotharakos, Z. Wadiasingh, A.K. Harding and D. Kazanas, *The multipolar magnetic field of the millisecond pulsar psr j0030+0451*, *The Astrophysical Journal* **907** (2021) 63.
- [25] J.S. Heyl and N.J. Shaviv, *Polarization evolution in strong magnetic fields*, *MNRAS* **311** (2000) 555 [[astro-ph/9909339](https://arxiv.org/abs/astro-ph/9909339)].
- [26] C. Wang and D. Lai, *Wave modes in the magnetospheres of pulsars and magnetars*, *Mon. Not. R. Astron. Soc.* **377** (2007) 1095.
- [27] H. Kubo and R. Nagata, *Determination of dielectric tensor fields in weakly inhomogeneous anisotropic media. II*, *J. Opt. Soc. Am.* **71** (1981) 327.
- [28] H. Kubo and R. Nagata, *Vector representation of behavior of polarized light in a weakly inhomogeneous medium with birefringence and dichroism*, *J. Opt. Soc. Am.* **73** (1983) 1719.
- [29] H. Kubo and R. Nagata, *Vector representation of behavior of polarized light in a weakly inhomogeneous medium with birefringence and dichroism. II. Evolution of polarization states*, *J. Opt. Soc. Am. A* **2** (1985) 30.
- [30] J.S. Heyl, N.J. Shaviv and D. Lloyd, *The high-energy polarization-limiting radius of neutron star magnetospheres — I. Slowly rotating neutron stars*, *MNRAS* **342** (2003) 134.
- [31] J. Heyl and I. Caiazzo, *Strongly Magnetized Sources: QED and X-ray Polarization*, *Galaxies* **6** (2018) 76.
- [32] O. Novak, M. Diachenko, E. Padusenko and R. Kholodov, *Vacuum Birefringence in the Fields of a Current Coil and a Guided Electromagnetic Wave*, *Ukrainian Journal of Physics* **63** (2018) 979.
- [33] D.-H. Kim and S. Trippe, *General relativistic effects on pulsar radiation*, arXiv e-prints (2021) [[2109.13387](https://arxiv.org/abs/2109.13387)].
- [34] R.D. Blandford and D.G. Payne, *Hydromagnetic flows from accretion discs and the production of radio jets*, *MNRAS* **199** (1982) 883.
- [35] R.T. Gangadhara, *On the method of estimating emission altitude from relativistic phase shift in pulsars*, *ApJ* **628** (2005) 923 [[astro-ph/0412705](https://arxiv.org/abs/astro-ph/0412705)].

- [36] G. Pavlov, O. Kargaltsev and B. Durant, M. Posselt, “X-ray Observations of Rotation Powered Pulsars.” https://www.cosmos.esa.int/documents/332006/943890/GPavlov_t.pdf, 2013.
- [37] NIST, “Digital Library of Mathematical Functions, National Institute of Standards and Technology, U.S. Department of Commerce.” <https://dlmf.nist.gov>, 2024.
- [38] G.B. Rybicki and A.P. Lightman, *Radiative processes in astrophysics*, John Wiley & Sons (1991).
- [39] M.O. Scully and M.S. Zubairy, *Quantum optics*, Cambridge University Press (1997).
- [40] J.A. Gil and J.K. Snakowski, *Curvature radiation and the core emission of pulsars*, *Astronomy and Astrophysics* **234** (1990) 237.